



Available online at www.keaipublishing.com/en/journals/journal-of-magnesium-and-alloys/

ScienceDirect

Journal of Magnesium and Alloys 13 (2025) 3596-3616



www.elsevier.com/locate/jma

Full Length Article

Anodic behaviour of Mg at pre-breakdown stages of PEO in basic electrolytes

Yuchen Lu^{a,b}, Aleksey Rogov^{a,b}, Sepideh Aliasghari^{a,b}, Aleksey Yerokhin^{a,b,*}

^a Department of Materials, University of Manchester, Oxford Road, Manchester M13 9PL, UK

^b Henry Royce Institute, Royce Hub Building, Oxford Road, Manchester M13 9PL, UK

Received 21 March 2025; received in revised form 5 June 2025; accepted 21 June 2025 Available online 5 August 2025

Abstract

Electrolyte selection for Plasma Electrolytic Oxidation (PEO) of magnesium is important as this determines composition, morphology and properties of resultant coatings that are urgently sought after for protection of Mg alloys from corrosion and wear in harsh environments. However, electrolyte design is often performed heuristically, which hampers the development and optimisation of new PEO processes. Here, we attempt to achieve a mechanistic understanding of electrochemical and microstructural aspects of anodic films evolution at the pre-breakdown stages of PEO treatments of magnesium in aqueous alkaline solutions of NaAlO₂, Na₃PO₄, NaF and Na₂SiO₃. Systematic studies have shown that magnesium self-passivation by MgO/Mg(OH)₂ can be compromised by both chemical and mechanical instabilities developed due to side effects of anodic reactions. Stable initiation of PEO process requires maintaining surface passivity in a wide range of pH, which can be achieved only by combining self-depositing passivators with those binding dissolved magnesium into insoluble compounds.

© 2025 Chongqing University. Publishing services provided by Elsevier B.V. on behalf of KeAi Communications Co. Ltd.

This is an open access article under the CC BY-NC-ND license (http://creativecommons.org/licenses/by-nc-nd/4.0/)

Keywords: Magnesium; Plasma electrolytic oxidation; High-voltage voltammetry; Passivity breakdown.

1. Introduction

Weight reduction is the most efficient means of increasing energy efficiency in automotive and aerospace industry. Magnesium alloys provide high strength-to-weight ratio rendering them attractive for lightweighting purposes [1–3]. However, the major limitation of Mg based materials comprises high chemical reactivity which aggravates in-service degradation of Mg components operating under harsh environmental conditions. To address this issue, protective coatings and chemical conversion treatments can be applied to the component surface.

Anodising is a well-established technique to electrochemically grow oxide films on the surfaces of light alloys, typically in solutions of strong acids. Despite strong adhesion to the metal substrate [4], amorphous anodic oxide films can-

E-mail address: Aleksey. Yerokhin@manchester.ac.uk (A. Yerokhin).

not offer sufficient protection from wear and corrosion attack hence additional post-treatments are needed [5,6]. In contrast, Plasma Electrolytic Oxidation (PEO) is typically performed in dilute alkaline solutions, which is particularly suitable for Mg alloys and significantly reduces environmental risks, offering a greener alternative to conventional anodising. PEO treatments are carried out at higher than anodising cell voltages (300-600 V), which results in localised dielectric breakdown of the growing anodic film manifested in the appearance of microdischarges at the film surface. The local instantaneous temperature and pressure developed in the microdischarges can be sufficiently high to promote crystallisation and high temperature phase transformations in the oxide layers [7,8]. Resulting coatings can therefore deliver enhanced properties such as high wear and corrosion resistance as well as offer good thermal and electrical insulation [9–11].

Formation of stable passive films at the pre-breakdown stages of PEO processing is crucial for enabling steady initiation and uniform spatial distribution of microdischarge events. Delayed microdischarge initiation is usually indicative of cor-

[☆] Peer review under the responsibility of Chongqing University.

^{*} Corresponding author.

rosion damage to the anodic oxide film, which significantly reduces quality of surface finish and protective properties of produced coatings. PEO coatings formed in uninhibited alkaline solutions comprise mainly MgO which cannot completely cover the metal surface because low Pilling Bedworth ratio, 0.81 < 1, leaving it exposed to chemical attack. Therefore, passivating agents such as silicate [12–14], various phosphates [15,16], aluminate [17] or fluoride [18,19] are often added to alkaline electrolytes to facilitate formation of insoluble protective compounds. By modifying electrolyte, coating composition can be tailored to enhance its protective properties. For example, PEO treatments in silicate alkaline solutions are known to result in formation of chemically stable magnesium orthosilicate (Mg₂SiO₄) phase with high corrosion resistance [20,21]. Phosphate additions enable compact PEO coatings on magnesium to be obtained [22,23], whereas aluminate is favourable for the formation of hard spinel (MgAl₂O₄) [24] and alumina (Al₂O₃) [25] phases promoting coating wear resistance [26,27]. Additions of fluorides enable thin layers of insoluble MgF₂ to be developed at the metal-film interface, which serves as a superior protective barrier against corrosion [28–30]. Complex electrolytes combining several additions have recently been explored for rapid 'flash' PEO processing of Mg [23]. However, the electrolytes used were not efficient in stable process initiation without additional pretreatments, which compromised the benefits brought by this promising approach.

Although passivating additions are recognised for providing enhanced coating performance, they may affect the initiation of PEO process in different ways. It has been suggested that the concentration of oxyanions in the vicinity of the anode has an impact on the breakdown voltage and discharging behaviour during PEO treatment [31]. In addition, stability of insoluble phases comprising anodic films on Mg depends on passivator concentration and local pH value which can deviate from the bulk solution pH due to electrochemical reactions resulting in the local acidification caused by anodic current [32,33]. The magnitude of local pH deviation is strongly influenced by buffering capacity of electrolyte solution, which depends on the range of acid-base equilibria available in the PEO electrolyte. Moreover, the local pH value in respect of isoelectric point of the insoluble compound in the film may affect the surface charge and electrical response of the electrode [34]. This presents numerous challenges in currently prevailing heuristic approaches to electrolyte formulation, which impedes the development of new PEO processes for high-performance coatings.

Long standing problems with rationalisation of electrolyte design for PEO treatments of Mg are caused by a lack of systematic understanding of chemical and electrochemical processes taking place at pre-breakdown stages of anodic film growth and their links with microstructural evolution of resulting PEO coatings. In this work, we have carried out linear sweep voltammetry studies of anodic behaviour of commercially pure magnesium (cp-Mg) in basic electrolyte systems comprising aqueous alkaline solutions of NaAlO₂, Na₃PO₄, NaF and Na₂SiO₃, in a broad range of potentials covering

pre- and post-breakdown stages of PEO coating growth. Produced polarisation curves were analysed using solubility data for solid compounds of magnesium and/or electrolyte constituents, combined with advanced microstructural, chemical and phase analyses of the films formed in characteristic voltage regions. Results of this study will assist in rational design of electrolyte systems for PEO treatment of magnesium, enabling stable initiation of microdischarge and formation of high-performance coatings.

2. Experimental

2.1. High-voltage voltammetry

Commercially pure Mg rods (Alfa Aesar; composition (wt %): Mg 99.826; Mn, Si, Co < 0.05; Al, Cu < 0.005; Fe, Pb, Ni, Zinc, <0.001 each) were cut into samples with dimensions of 19 mm \times 19 mm \times 6 mm providing the exposed surface area $A=11.78~\rm cm^2$. The samples were ground by up to #800 grit SiC papers to Ra \sim 0.2 μ m and stored under a layer of absolute ethanol preventing contact with air before processing.

The process was carried out in four different electrolytes: NaAlO₂ (technical grade, Sigma-Aldrich), Na₃PO₄ (laboratory grade, Fluorochem), NaF (laboratory grade, Alfa Aesar) and Na₂SiO₃ (general purpose grade, Fisher Scientific UK). Solution pH level was adjusted to 13.00 by the addition of KOH (analytical grade, Fisher Scientific). Initial survey scans were carried out in electrolytes with concentrations ranging from 0.025 M to 0.1 M, with further detailed investigation performed in the regions of interest identified in obtained voltammograms.

Anodic polarisation was provided by an MDXII (Advanced Energy Industries, Inc) DC power supply operated in a voltage ramp mode. A National Instruments PXI-5922 analogue-to-digital converter interface module was used for data acquisition from Tektronix TCPA300 current probe and P5200A voltage probe. One data point was recorded every second as an average over 100 ms data acquisition interval. The voltage and current vs time dependencies were monitored through a Lab-VIEW script, with polarisation curves plotted subsequently as voltammograms in current density vs voltage coordinates.

Fig. 1 schematically illustrates the triangular voltage pulse for high-voltage voltammetry. Since the power supply used could only source current to the load and not to sink it, the actual downward part of the pulse deviated from the desired linear shape due to power supply capacitance affecting voltage output on high-impedance loads at low currents (Fig. 1a). However, the voltammetric response was not affected as the current during this period is almost absent. Linear voltammetric sweeps were carried up to a maximum voltage ($U_{\rm max}$) and down to zero, at rates of 2.66, 4.33, 6 and 7.67 V/s. The value of $U_{\rm max}$ was set up to be above the breakdown voltage ($U_{\rm BD}$) and corresponding to the point where the current density approaches the maximum value of $j_{\rm max} \sim 1~{\rm A/cm^2}$. The value of $U_{\rm BD}$ was determined as an intersect between the slopes of low- and high-voltage segments in the upward branch of the

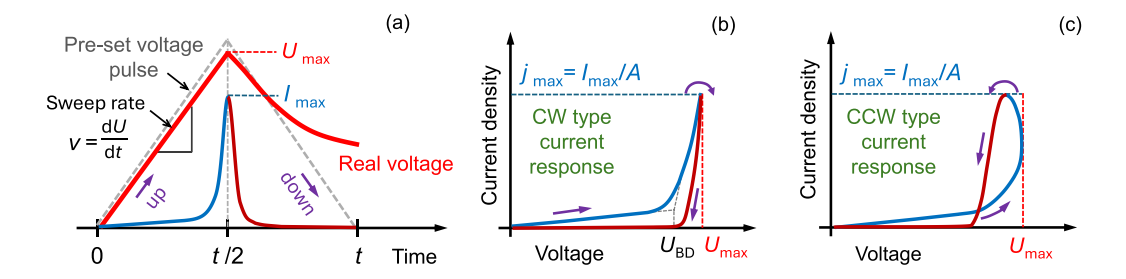


Fig. 1. Schematic presentation of the triangular voltage pulse for high-voltage voltammetry (a) and examples of voltammograms with clockwise (CW) (b) and counterclockwise (CCW) current response (c).

voltammogram (Fig. 1b), whereas visual observation of discharge events at that point was not always possible due to low transparency of some electrolyte solutions and/or shielding of sample surfaces by gaseous products of electrolysis. Fig. 1b and c illustrate two types of voltammetric response observed at $U_{\rm max}$, when switching from upward to downward branch of the pulse and denoted clockwise (CW) and counterclockwise (CCW) current response, respectively.

Solubility analysis of anodic reaction products involving Mg substrate and electrolyte species was carried out using ChemEQL [35] using reference data from [36–38].

2.2. Materials characterisation

2.2.1. Surface analysis

Scanning electron microscopy (SEM) observations were performed in backscattered electron (BSE) imaging mode using a Tescan Mira3 SC microscope to observe the surface morphology of film generated on Mg substrate. Energy Dispersive X-ray Spectroscopy (EDS) was adopted to measure the film chemical composition, using Oxford Instruments 50 mm² X-Max EDS detector operated at 15 kV for sufficient electron beam/specimen interaction volume. The average elemental composition (in at.%) was acquired from a rectangular area of 1500 $\mu m \times 1300~\mu m$ of the film, with quantification achieved by referring to the Oxford Instruments' Aztec database of standardisations.

X-ray Photoelectron Spectroscopy (XPS) was performed using an Axis Ultra Hybrid spectrometer (Kratos Analytical, Manchester, United Kingdom) using monochromate Al K α radiation (1486.6 eV), which can detect the information of \sim 10–20 nm below the out most surface of the specimen. An electron flood gun was used for charge neutralisation. Binding energy scale calibration was performed using C–C in the C 1s photoelectron peak at 284.8 eV. Before collecting high-resolution spectra, monoatomic Ar etching source was used for 60 s to remove contamination from the surface. The NIST X-ray Photoelectron Spectroscopy Database [39] was referred for the analysis with curve fitting performed using CasaXPS software.

For selected samples treated in silicate solutions, Raman spectroscopy analysis was also performed using a Renishaw 1000 spectrometer operated under ambient conditions. The spectra were taken at a laser wavelength of 532 nm and a

power of 36.6 mW, using \times 50 objective lens, which resulted in a laser beam size of \sim 1 μ m on the specimen surface.

2.2.2. Cross sectional analysis

Elemental depth profiling of the surface layer was investigated by glow discharge optical emission spectroscopy (GDOES) using a GD-Profiler 2 (Horiba Jobin Yvon) at Ar pressure of 635 Pa and pulsed power 8.75 W (frequency = 500 Hz, duty cycle = 0.25).

Lamellas originated from individual films were prepared by Focused Ion Beam (FIB) using FEI Nova Nanolab 600, which were subsequently used for High Angle Annular Dark Field (HAADF) Scanning Transmission Electron Microscope (STEM) imaging, EDS maps and line scans, accomplished by FEI Talos F200A Transmission Electron Microscope (TEM) operated at 200 kV to study the cross-sectional morphology and composition of anodic films.

2.2.3. Phase analysis

Grazing incidence X-ray Diffraction (GIXRD) analysis was performed by a Bruker D8 Discover Autochanger diffractometer using a Cu K α radiation source ($\lambda = 1.5418$ Å), aiming at reducing the interference from the underlying Mg substrate while enhancing the sensitivity to phases within the surface film. The scans were caried out at 1° grazing angle from 15° to 80° 2 θ , with a step size of 0.02° and dwell time 2 s per step.

3. Results

3.1. Effect of electrolyte concentration on anodic behaviour of cp-Mg

Survey voltammograms and surface appearances of corresponding cp-Mg samples obtained in individual electrolytes with various concentrations are shown in Fig. 2a and b respectively. In the upward branches of voltammograms, when the applied voltage does not exceed 100 V the current is generally about 50 mA/cm², which can be attributed to the conventional anodisation stage. Above 100 V, the voltammograms show different trends depending on electrolyte composition and concentration. In aluminate (Fig. 2, Ia) and fluoride (Fig. 2, IIa) electrolytes, the passivity is followed by a noticeable active behaviour forming characteristic current peaks,

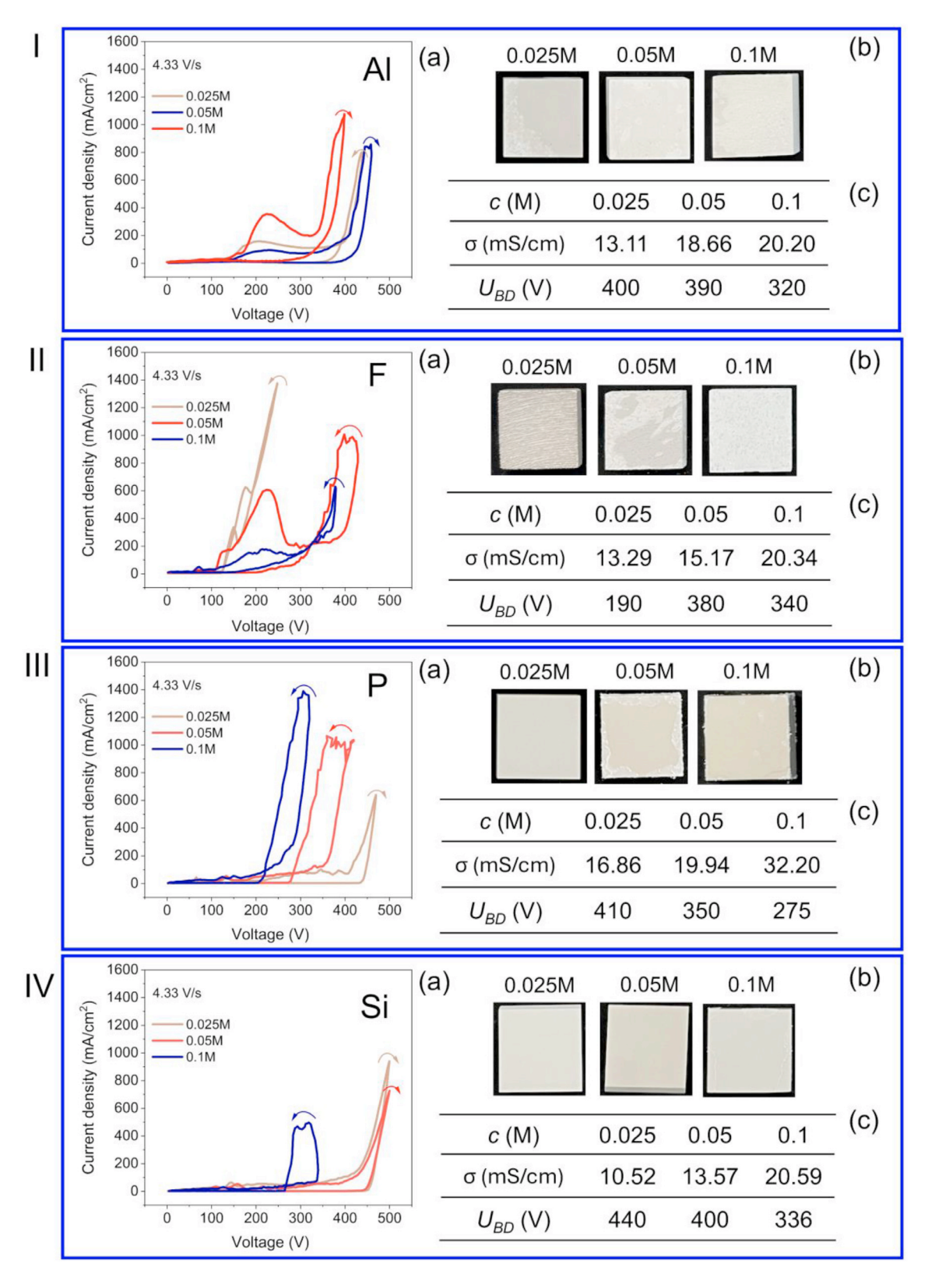


Fig. 2. High-voltage voltammograms obtained at a sweep rate of 4.33 V/s, illustrating anodic behaviour of cp-Mg in alkaline solutions (pH=13) with different concentrations of additions: Al – aluminate, F – fluoride, P – phosphate, Si – silicate (a); surface appearance of samples after the voltammetry experiments (b) and values of conductivity (σ) and breakdown voltage ($U_{\rm BD}$) in individual electrolyte systems with various concentrations (c).

albeit with some differences. In the aluminate solution, the current peak centred at about 220 V is the most pronounced at the highest aluminate concentration (0.1 M), whereas it is depressed to a plateau in more dilute solutions. In fluoride solutions, the most active behaviour is observed at the lowest electrolyte concentration 0.025 M, where current quickly reaches the maximum pre-set value, whereas a broad shallow hump is developed at 0.1 M. At the intermediate concentration (0.05 M), the active region begins with a shoulder formed at ~150 V followed by a pronounced peak with a summit at about 220 V, whilst further increase in voltage (>290 V) leads to a current plateau at ~230 mA/cm². In contrast, phosphate (Fig. 2, IIIa) and silicate (Fig. 2, IVa) electrolytes demonstrate only slow increases in current density up to high voltages, with very small current peaks (<100 mA/cm²) observed at 130 V and 160 V respectively. In the high-voltage regions, the values of breakdown voltage beyond which the current starts increasing dramatically show a rather strong correlation with electrolyte conductivity ($U_{\rm BD} = 790 - 339 \cdot \log_{10} \sigma$, $R^2 = 0.85$) for all but 0.025 M fluoride electrolyte (Fig. 2c). This is consistent with the empirical relationship well known for anodic films on valve metals [40]. The slopes of highvoltage branches vary within 0.88 to 2.18×10^{-2} (A/(V·cm²)) range indicating different throwing power of the studied electrolytes, which usually determines film uniformity.

In all fluoride solutions, transition to the downward branches of voltammograms occurs with a counterclockwise current response. However in other electrolyte systems, it changes with the increase in electrolyte concentration either from CCW to CW type behaviour in aluminate solutions, or the other way around in phosphate and silicate solutions. Visual observations of sample surfaces after voltammetry experiments (Fig. 2b) reveal that the CW response generally correlates with uniform surface appearance. In the case of CCW type however, large rough precipitates or excessive depositions were formed near the edges of samples treated in 0.025 M aluminate, 0.05 M fluoride and phosphate as well as in 0.1 M phosphate and silicate electrolytes. Based on both voltammogram features and sample surface appearances, 0.1 M NaAlO₂ and 0.05 M solutions of NaF, Na₃PO₄ and Na₂SiO₃ were selected for detailed investigation.

3.2. Effect of voltage sweep rate on anodic behaviour of cp-Mg

The voltammograms in Fig. 3a illustrate effects of voltage sweep rate on anodic behaviour of magnesium in selected electrolytes. In aluminate (Fig. 3, Ia) and fluoride electrolytes (Fig. 3, IIa) the magnitudes of active peaks at about 220 V increase progressively with the sweep rate. Current vs charge analysis shows that positions of these peaks are independent of sweep rate corresponding to approximately the same charge, 56 ± 1 C for aluminate (Fig. 3, Ib) and 107 ± 3 C for fluoride electrolyte (Fig. 3, IIb). Thus, repassivation may be associated with the increase in surface coverage by means of a Faradaic process, which is not sensitive to the voltage sweep rate within the given range.

By the end of post-breakdown stage where the voltage is at its maximum, the increase in sweep rate leads to a higher value of the maximum current in the aluminate (Fig. 3, Ib) and silicate electrolytes (Fig. 3, IVb), both of which feature a CW response in the downward branch of the voltammogram. However, in electrolyte systems that exhibit the CCW response, the maximum current either decreases (in fluoride electrolyte, Fig. 3, IIb) or remains at approximately the same level (in phosphate electrolyte, Fig. 3, IIIb) when the sweep rate increases. Such phenomena can be attributed to the stability of the passive state associated with precipitation of different insoluble compounds. For instance, lower sweep rates are translated into longer polarisation times and charge passed may be higher, which results in a higher accumulated proton concentration at the vicinity of the anode, hence in a lower local pH. On one hand, this promotes formation of self-depositing compounds like hydrated silica or alumina so that the surface film obtains higher barrier properties, thus lowering the current (Fig. 3, Ib, IVb). On the other, local acidification significantly reduces the film stability by promoting dissolution of Mg(OH)₂ and Mg₃(PO₄)₂ for fluoride and phosphate solutions, respectively. In the case of phosphate electrolyte (Fig. 3, IIIb), almost constant current peak magnitudes can be explained by the buffering properties of this solution, which is not the case for fluoride one.

3.3. Characteristics of anodic films

3.3.1. Aluminate solution

3.3.1.1. Stage 0-1: anodisation. In aluminate electrolyte, initial anodisation takes place below 150 V and the current density (i) does not exceed 30 mA/cm² (Fig. 4, Ia). SEM observations reveal that the surface is covered with a uniform film without apparent defects, which is composed mainly by magnesium and oxygen, with a minor content of Al, detected by the aera averaged EDS analysis (Fig. 4, Ib). Minor (<1%) amounts of Na and K originated from the electrolyte and detected in the film were normally discarded from quantification. More details can be revealed with XPS, where Mg 2p peak at binding energy 49.95 eV can be attributed to Mg-O bond in Mg(OH)₂ (Fig. 4, IIa); Al 2p peak at binding energy 73.90 eV can be associated with Al-O bond in Al(OH)₃, whereas the peak at 74.20 eV can be attributed to Al-O in boehmite (AlOOH) (Fig. 4, IIb). This is also in agreement with GDOES profile (Fig. 4, IIIa), which reveals high relative contents of H and O within the bulk of the film, indicating that it predominantly consists of hydrated compounds. For Al, the intensity of GDOES signal gradually decreases from the surface to the substrate. Considering the above analysis, it can be concluded that the structure of the initial passive film is mainly Mg(OH)₂ with small amounts of Al(OH)₃ at the film-electrolyte interface.

3.3.1.2. Stage 1–2: activation. Further increase in applied voltage above 150 V is accompanied by a sharp current increase up to the peak value of $j \sim 350 \text{ mA/cm}^2$ at 220 V, indicating active behaviour. The film turns into a flaky struc-

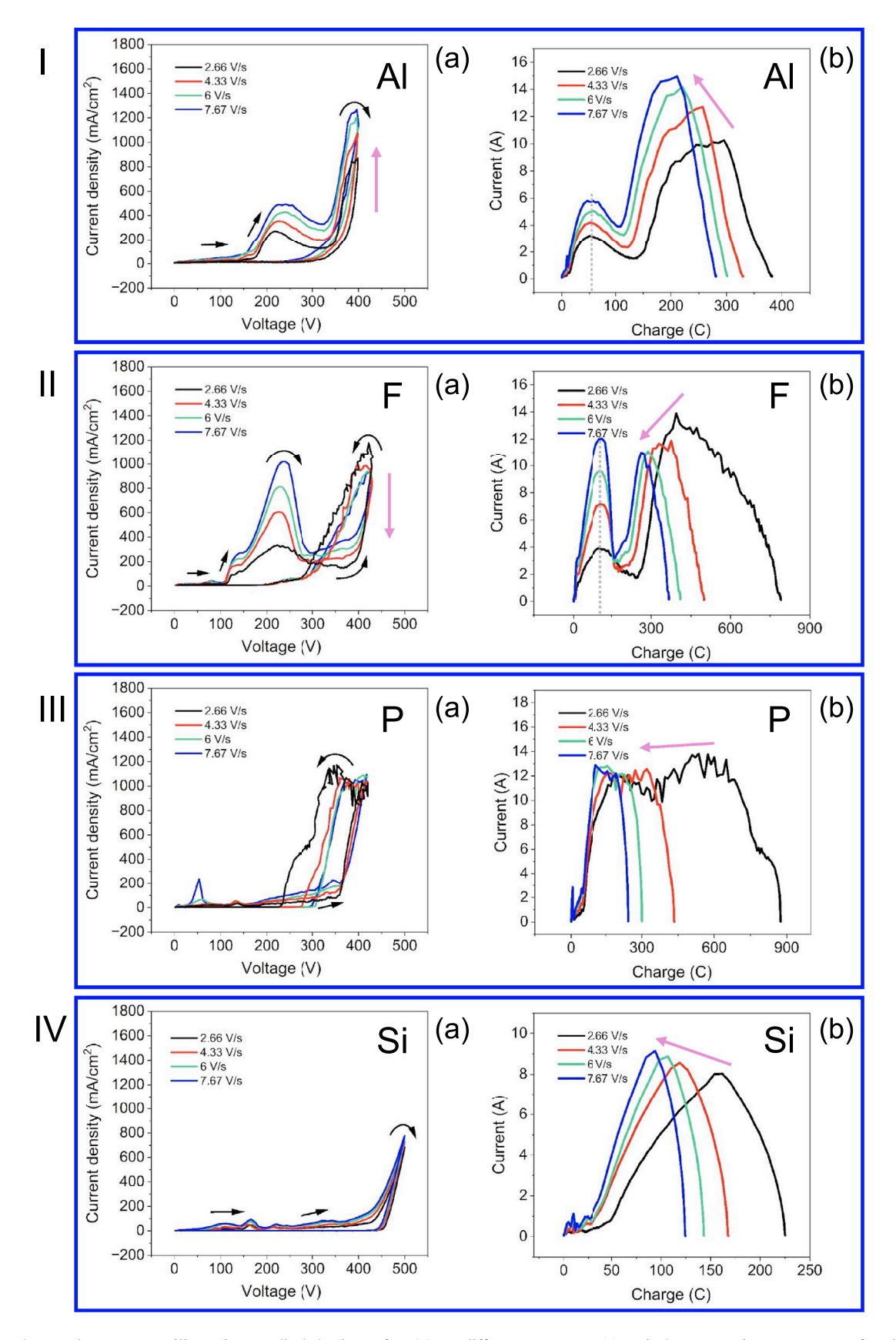


Fig. 3. High-voltage voltammograms illustrating anodic behaviour of cp-Mg at different scan rates (a) and plots presenting current as a function of passed charges (b) in various electrolyte systems (for notations see caption of Fig. 2).

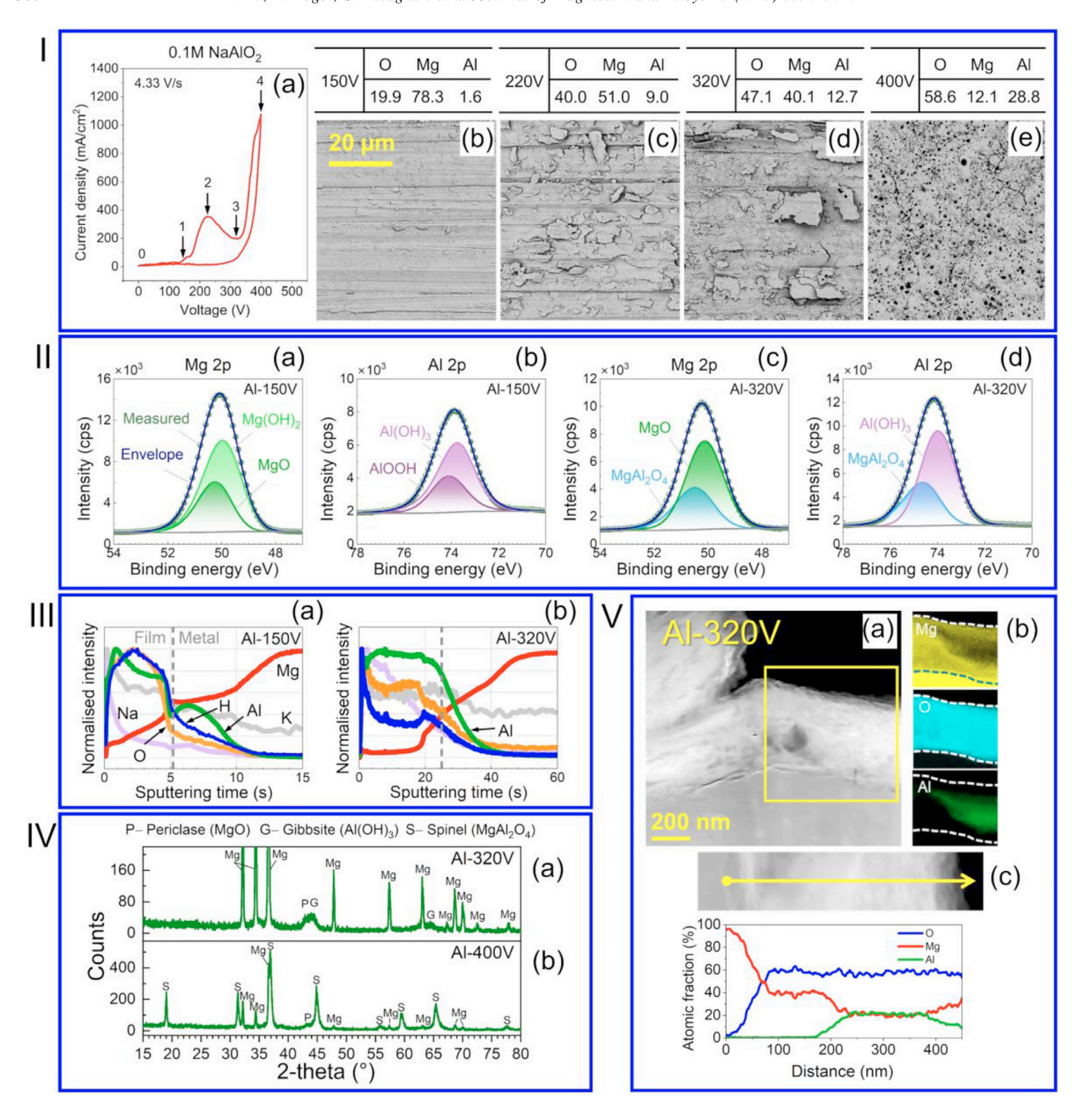


Fig. 4. Voltammogram for magnesium in 0.1 M NaAlO₂ solution at the sweep rate of 4.33 V/s (Ia), surface morphology and chemical composition of the films formed at different voltages (Ib-e); XPS spectra of the core levels of Mg and Al elements contained in the film formed at 150 V (IIa, b) and 320 V (IIc, d); GDOES profiles for the film at 150 V (IIIa) and at 320 V (IIIb). (K and Na elements are in faded colour); XRD patterns of the film formed at 320 V (IVa) and 400 V (IVb) (Mg denotes peaks from Mg substrate); TEM evaluation of the pre-breakdown film on magnesium in cross section (Va), elemental maps (Vb) and EDS line scans (Vc) for substrate magnesium and anion main elements.

ture with flake size of \sim 7–10 μ m (Fig. 4, Ic), which is enriched with oxygen and aluminium and shows a decrease in magnesium content evident from EDS analysis. The flakes are partly delaminated violating passivity of the film at this stage, however, further increase in voltage results in repassivation.

3.3.1.3. Stage 3: repassivation. The voltage growth above 220 V leads to a decrease in the current density to a minimum value (\sim 195 mA/cm²) at \sim 320 V, above which the breakdown is initiated. The film formed at the pre-breakdown stage (220 < U < 320 V) exhibits coarser flakes on the surface (\sim 15–20 μ m, Fig. 4, Id), with increased aluminium content

(12.7%). From XRD results (Fig. 4, IVa), the film contains gibbsite (Al(OH)₃) and minor amounts of periclase (MgO). Based on XPS observations (Fig. 4, IIc, d), the Mg 2p binding energy 50.50 eV fits the Al-O bond in spinel (MgAl₂O₄), which is also in agreement with the chemical environment of aluminium in spinel as evidenced by the signal at 74.70 eV in Al 2p spectrum. In the cross-sectional TEM image (Fig. 4, Va), the film exhibits a relatively dense structure without apparent defects such as pores or cracks. From the elemental maps (Fig. 4, Vb), it can be observed that O is uniformly distributed throughout the film thickness. However, Mg exhibits higher concentration at both metal-film and film-electrolyte interface, but the middle part of the film is predominantly enriched with Al, forming a sandwich-like structure. Considering film phase composition comprising MgO and Al(OH)₃ (that are also detected by XPS) and the EDS line scan (Fig. 4, Vc), the layers can be identified as follows: a) the sub-layer adjacent to the metal-film interface mainly consists of MgO which is partly hydrated near to metal-film interface, consistent with a higher H content in GDOES profile (Fig. 4, IIIb); b) the sub-layer in the middle of the film consists mainly of Al(OH)₃; c) the top most sub-layer enriched both in Mg and Al as well as in hydrogen is probably a mixture of amorphous Mg(OH)₂ and Al(OH)₃ compounds.

3.3.1.4. Stage 3–4: breakdown. The increase in voltage above 320 V is associated with rapid current increase to a high value ($j \sim 1100 \text{ mA/cm}^2$) and visible sparks that can be detected on the surface. This results in a fused morphology with round crater-like pores, which is typical for PEO coatings (Fig. 4, Ie). Its surface composition now demonstrates the decrease in Mg content, while Al continuously increases up to 28.8%. The XRD pattern (Fig. 4, IVb) shows that spinel now is the dominant phase in the film. Thus, we believe that previously formed MgO and Al(OH)₃ phases can react with each other under the breakdown conditions, yielding MgAl₂O₄.

3.3.2. Fluoride solution

For fluoride solution, the sweep rate of 6 V/s was chosen for detailed investigation to emphasise a small current peak at 80 V which is almost negligible at lower scan rates. This is believed to only affect the kinetics of anodic process while underlying mechanisms remain the same.

3.3.2.1. Stage 0–1: anodisation. After the initial voltage increase, the current in the fluoride electrolyte shows a local maximum of 40 mA/cm² at 80 V, followed by a decrease to the initial level (~ 20 mA/cm²) at 100 V (Fig. 5, Ia). A uniform film grows on the magnesium substrate (Fig. 5, Ib), with 80.5% Mg and 16.2% O as well as minor fluoride (3.3%) in its composition measured by EDS. As evidenced by XPS (Fig. 5, IIa), the film comprises of MgO where Mg 2p peak is centred at 50.25 eV and Mg(OH)₂ peak at 49.95 eV, which is consistent with the GDOES depth profile (Fig. 5, IIIa) illustrating a correlative distribution of H and O within the bulk of the film. The fluoride is concentrated at the electrolyte-film

interface and its content gradually decreases towards the substrate. This is supported by the XPS where the Mg 2p peak at 50.90 eV (Fig. 5, IIa) and F 1s peak at 685.40 eV (Fig. 5, IIb) can be associated with MgF $_2$. We can conclude here that the film is a homogeneous mixture of MgO, Mg(OH) $_2$ and MgF $_2$.

3.3.2.2. Stage 1–2: activation. As the applied voltage rises above 100 V, the current density sharply increases to a peak of 225 mA/cm² at about 150 V forming a shoulder in the voltammogram. Such active behaviour resulted in the surface morphology featured by granular deposits separated by deep protrusions. More details can be observed on a tilted specimen (Fig. 5, Ic insert) at higher magnification, which shows a columnar structure, with pillars of 5 μm in height and 0.5 μm in diameter. From EDS analysis of the surface, it contains a slightly increased content of O (19.2%) and F (7.0%) at a decreased content of Mg (19.2%) in respect to the previous stage. Such morphology can be associated with intensive dissolution of the metal substrate underlying the initial film formed below 100 V.

3.3.2.3. Stage 2–3: active-passive transition. When the voltage exceeds 150 V, the current density increases again up to a peak value of $\sim 810~\text{mA/cm}^2$ at 225 V and then decays back to 250 mA/cm² at 290 V. The surface inherited deep protrusions from the previous stage (Fig. 5, Id) with slightly larger granules ($\sim 5~\mu \text{m}$). Looking them into details, we can see the crystals with leaf-like appearance (Fig. 5, Id inset). As it was difficult to prepare the lamella from the region with columnar deposits, the cross-sectional characterisation was carried out for the uncorroded site, however, other characterisation techniques represent the average surface properties including those features. The cross-section of the film shows compactness although many closed pores can be observed (Fig. 5, Va).

The elemental maps (Fig. 5, Vb) show that the region adjacent to the metal-film interface is enriched by F and depleted by O, which is in agreement with F profile in GDOES (Fig. 5, IIIb) and EDS line scan (Fig. 5, Vc) indicating F-rich band of about 150 nm. In addition, the H signal near the metal-film interface indicating low content of hydrated phases. Thus, the interfacial layer contains a mixture of MgF₂ and MgO at a ratio of about 1:1.

The remainder of the film shows a relatively uniform distribution of both Mg and O (Fig. 5, Vc), but there is a significant decrease in F towards the film-electrolyte interface where H is concentrated as revealed by GDOES analysis (Fig. 5, IIIb). The latter indicates a presence of hydrated phases at the film-electrolyte interface, which is also evidenced by Mg 2p peak at 49.95 eV attributed to Mg–O bond in Mg(OH)₂ (Fig. 5, IIc). Thus it should be only attributed to the columnar deposits.

As detected by XRD (Fig. 5, IVa), periclase (MgO), brucite (Mg(OH)₂) and sellaite (MgF₂) phases are found at the surface. Based on the above analysis, we can conclude that Mg(OH)₂ is predominantly present in the columnar deposits,

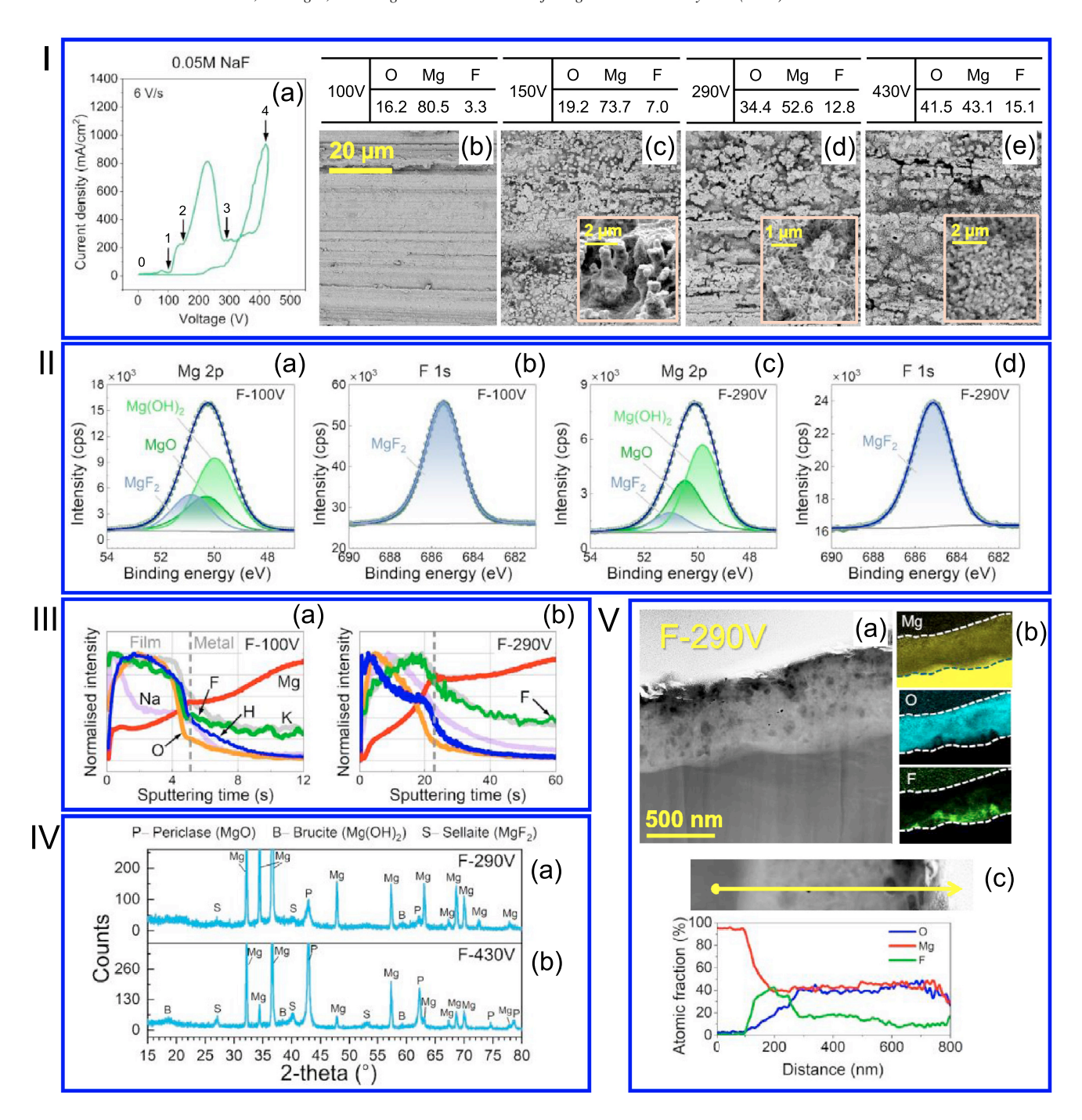


Fig. 5. Voltammogram for magnesium in 0.05 M NaF at the sweep rate of 6 V/s (Ia), surface morphology and chemical composition of the films formed at different voltages (Ib-e); XPS spectra of the core levels of Mg and F elements contained in the film formed at 100 V (IIa,b) and 290 V (IIc, d); GDOES profiles for the film at 100 V (IIIa) and at 290 V (IIIb). (K and Na elements are in faded colour); XRD patterns of the film formed at 290 V (IVa) and 430 V (IVb) (Mg denotes peaks from Mg substrate); TEM evaluation of the pre-breakdown film on magnesium in cross section (Va), elemental maps (Vb) and EDS line scans (Vc) for substrate magnesium and anion main elements.

whereas the uncorroded film mainly consists of MgO and MgF_2 .

3.3.2.4. Stage 3–4: breakdown. The growth of voltage from 290 V to 370 V is accompanied by a gradual increase in current density, which is then dramatically increases to the peak value of about 930 mA/cm² at 430 V. At this stage, dielectric breakdown of the film occurs which causes the generation

of visible microdischarges. As a result, the film is featured by craters with round pores (Fig. 5, Ie). It is noticeable that the previously existing protrusions in the pre-breakdown film are now partly filled by granular precipitates surrounding the craters, leading to further increase in compactness of the film. After the breakdown, the film consists of increased amounts of crystalline MgO and MgF₂, as revealed by XRD analysis (Fig. 5, IVb).

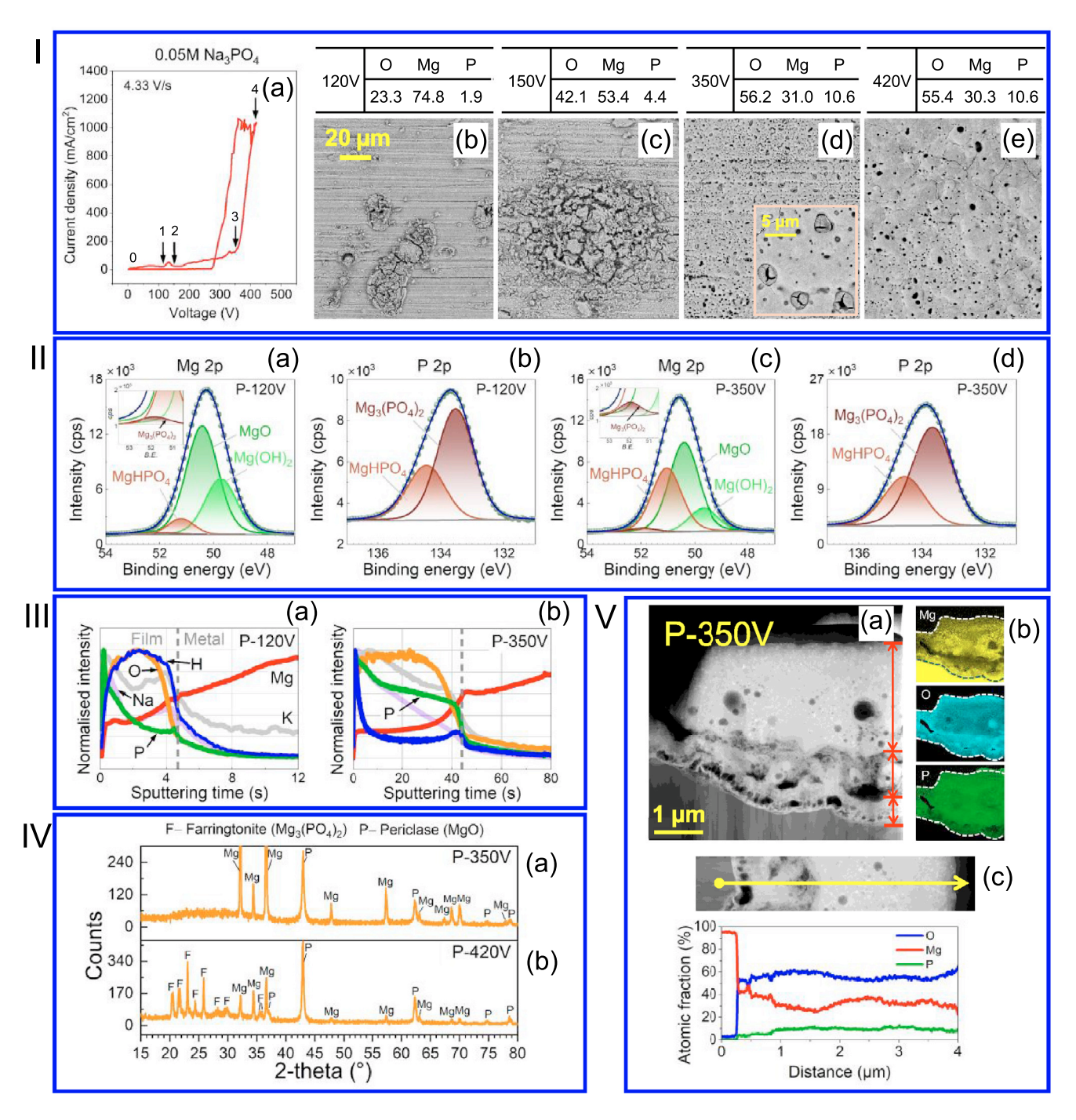


Fig. 6. Voltammogram for magnesium in 0.05 M Na_3PO_4 solution at the sweep rate of 4.33 V/s (Ia), surface morphology and chemical composition of the films formed at different voltages (Ib-e); XPS spectra of the core levels of Mg and P elements contained in the film formed at 120 V (IIa, b) and 350 V (IIc, d); GDOES profiles for the film at 120 V (IIIa) and at 350 V (IIIb). (K and Na elements are in faded colour); XRD pattens of the film formed at 350 V (IVa) and 420 V (IVb) (Mg denotes peaks from Mg substrate); TEM evaluation of the film formed on cp-Mg at breakdown voltage, in cross section (Va), elemental maps (Vb) and EDS line scans (Vc) for substrate magnesium and anion main elements.

3.3.3. Orthophosphate solution

3.3.3.1. Stage 0–1: anodisation. As initial anodisation proceeds up to 120 V in the phosphate electrolyte, the current density slowly increases and remains as low as 30 mA/cm² (Fig. 6, Ia). The surface morphology (Fig. 6, Ib) is represented by a relatively uniform layer containing mainly magne-

sium and oxygen (81.8% and 17.4%, respectively) with small amounts of P (0.8%). However, some islands (20–30 μ m) of a granular structure can be found to be randomly distributed across the surface. Their chemical composition is enriched with P (8.5 at.%) and oxygen (56.7%) at the expense of Mg content (34.5%). The chemical bonding determined by XPS

shows that in Mg 2p spectrum (Fig. 6, IIa), Mg–O bond can be associated with both MgHPO₄ (51.10 eV) and Mg₃(PO₄)₂ (51.90 eV) that are also evident in P 2p spectrum (peaks at 134.5 eV and 133.5 eV, respectively (Fig. 6, IIb). In addition, the Mg 2p peak at 49.95 eV indicates the formation of Mg(OH)₂. The GDOES depth profile (Fig. 6, IIIa) illustrates a correlative distribution of H and O throughout the film thickness, which is consistent with Mg(OH)₂. For P profile, phosphates are found to be concentrated at the film-electrolyte interface, and the content drops significantly towards the substrate. We assume that magnesium exhibits a primary passivation through formation of Mg(OH)₂ which is accompanied by its simultaneous reaction with phosphate, resulting in a local deposition of corrosion products (to be discussed in Section 4.2.3).

3.3.3.2. Stage 1–2: initial instability. As the process goes on, the current experiences a noticeable increase within a narrow voltage range of 120–150 V up to the maximum value of \sim 53 mA/cm², which is followed by a decrease to the passivation current of \sim 24 mA/cm². The surface morphology (Fig. 6, Ic) shows that phosphate enriched products cover larger area of the surface at this stage, which is also indicated by increased overall content of O (42.1%) and P (4.4%), as revealed by EDS. Summarising, during initial stages 0–2 anodic Mg(OH)₂ film experiences continuous transformation into more stable phosphate containing phases.

3.3.3.3. Stage 2–3: activation. Further increase in applied voltage up to 350 V is accompanied by gradual current increase to a higher value (\sim 135 mA/cm²). The film now exhibits a surface with numerous round micro-pores (Fig. 6, Id). It can be seen that the larger pores with \sim 3 μ m in diameter are filled with a new material featured by propagated cracks (Fig. 6, Id inset). The appearance of rounded features inevitably requires the material to be in a viscous state, which can be either a molten phase or a clay-like gel formed from highly hydrated phases under pre-breakdown conditions.

As shown by EDS (Fig. 6, Id), the amount of P and O elements in the film at this stage progressively increases, which is in agreement with XRD pattern indicating the presence of periclase (MgO) as well as a broad hump in the range of 20 to $37^{\circ} 2\theta$, which is assumed to be amorphous phosphate phases (Fig. 6, IVa). As identified by XPS (Fig. 6, IIc, d), chemical environment of phosphorus and magnesium is consistent with Mg₃(PO₄)₂ and MgHPO₄.

On a cross-sectional view (Fig. 6, Va) the film can be subdivided into three sub-layers: a) the interfacial barrier layer with a succession of voids along the metal/oxide boundary; b) a middle layer exhibiting sponge structure with foam-like tiny pores; c) an outer layer of dense and compact material containing round shape closed porosity.

As shown by the elemental maps (Fig. 6, Vb), Mg is concentrated at the metal-film interface. It is also noticeable in the GDOES profile (Fig. 6, IIIb) that H content shows a local maximum at the metal-film interface, which indicates the presence of hydrated phases. Combined with EDS line

scans data (Fig. 6, Vc), it is evident that the interfacial barrier layer mainly consists of MgO which is partly hydrated. The porous middle layer is depleted in Mg and enriched with P at the predominance of O, which can be attributed to a high content of magnesium phosphates as a result of dehydration (low H content in GDOES) occurring in this region under pre-breakdown conditions. The dehydration can also be considered as a potential reason for high level of observed porosity. In contrast, the outer layer contains higher amounts of Mg and P, as well as an enrichment of H noticeable in GDOES profiles (Fig. 6, IIIb). Therefore, we assume that the out most part of the film is enriched with hydrated substances, e.g. Mg(OH)₂ and MgHPO₄ that are also detected by XPS. However, there is a significant change in Mg:O stoichiometry, from 2.6 to 1.8, within the first 500 nm from the surface, which can be attributed to a higher content of dehydrated phases like MgO or Mg₃(PO₄)₂ deep into the outer layer. From GDOES profiles of P and H we can assume a predominance of MgHPO4 at the surface and MgO in the depth of the outer

3.3.3.4. Stage 3–4: breakdown. As the applied voltage increases from 350 V to 420 V, the current density experiences a sharp growth up to ~ 1030 mA/cm², which indicates a dielectric breakdown of the film, although some faint luminosity could already be visually detected at the activation stage. From the SEM image (Fig. 6, Ie), the resultant film exhibits a rough surface with numerous pores and microcracks indicative of a large heat released at this stage. Compared to the film generated at 350 V, the elemental composition is kept almost unchanged. However, from the XRD pattern (Fig. 6, IVb), a series of farringtonite (Mg₃(PO₄)₂) peaks is present in the range of 20° to 37° 2 θ , supporting our previous assumption about amorphous Mg₃(PO₄)₂ being formed during stage 2–3, which crystallises under discharge conditions.

3.3.4. Silicate solution

3.3.4.1. Stage 0–1: anodisation. In the silicate electrolyte, initial anodisation corresponding to the voltage region up to 70 V leads to a current density of 15 mA/cm² at maximum (Fig. 7, Ia). A uniform layer containing mainly magnesium (84.4%) and oxygen (14.9%) is developed on the substrate, with low content of silicon (0.7%) incorporated (Fig. 7, Ib). More details of the chemical state of silicon in the film can be revealed by XPS (Fig. 7, IIb) where signal at 102.20 eV and 102.85 eV of the chemical environment for the Si-O bond can be detected, which is attributed to $(SiO_2)_x(Na_2O)_y$ and SiO_2 , respectively. The former compound is related to electrolyte absorbed into the outer part of the film, which is consistent with traces of Na detected by EDS (see Section 3.3.1). In GDOES depth profile (Fig. 7, IIIa), the Si signal near the film-electrolyte interface indicates a high content of silicate phases whose amount significantly decreases within the bulk of the film. A correlative distribution of H and O and increased Mg signal towards the substrate indicates a high bulk content of Mg(OH)₂. However, the top surface is enriched with anhydrous phases, which is evidenced by Mg 2p

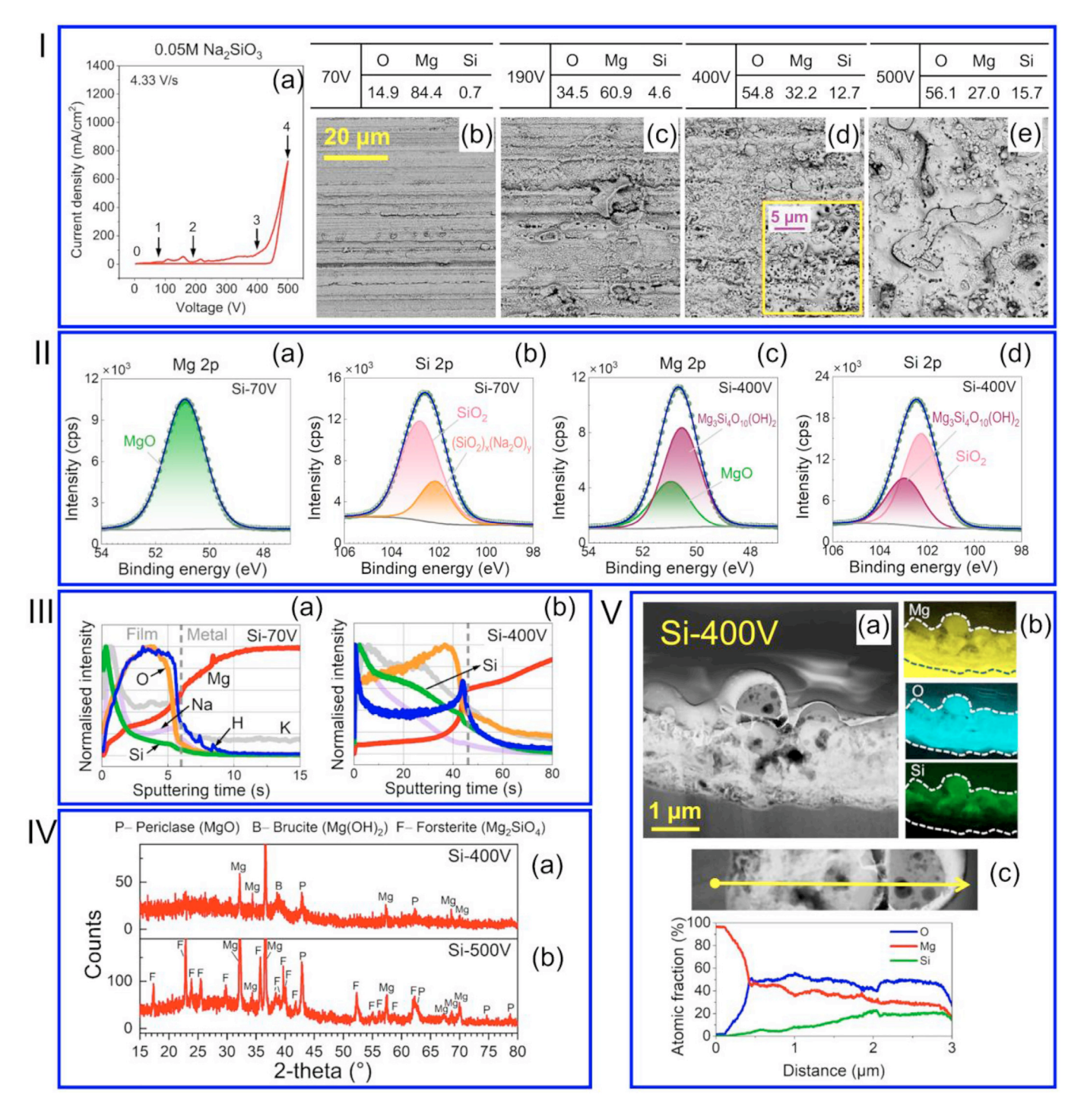


Fig. 7. Voltammogram for magnesium in $0.05 \text{ M Na}_2\text{SiO}_3$ solution at the sweep rate of 4.33 V/s (Ia), surface morphology and chemical composition of the films formed at different voltages (Ib-e); XPS spectra of the core levels of Mg and Si elements contained in the film formed at 70 V (IIa,b) and 400 V (IIc,d); GDOES profiles for the film at 70 V (IIIa) and at 400 V (IIIb). (K and Na elements are in faded colour); XRD pattens of the film formed at 400 V (IVa) and 500 V (IVb) (Mg denotes peaks from Mg substrate); TEM evaluation of the film on cp-Mg at the breakdown voltage, in cross section (Va), elemental maps (Vb) and EDS line scans (Vc) for substrate magnesium and anion main elements.

peak at 51.00 eV attributed the Mg-O bond in MgO (Fig. 7, IIa). Thus, the film structure is mainly $Mg(OH)_2$ with small amounts of SiO_2 distributed at the film-electrolyte interface.

3.3.4.2. Stage 1–2: initial instability. In the region of 70 to 190 V in the voltammogram, the current density undergoes

fluctuations forming two localised peaks: the first current peak is at a value of 30 mA/cm² at 110 V and the other is at 50 mA/cm² at 160 V. Subsequently, the current density decays back to the initial level (15 mA/cm²) once the voltage reaches 190 V. The surface morphology exhibits a uniform layer with O (32.0%), Mg (65.1%) and Si (2.8%) in its composition.

Also, some ring-like deposits ranging from 2 to 20 μm in diameter can be observed (Fig. 7, Ic) that are enriched with Si (13.6%) and O (66.1%) at decreased Mg content (20.1%). Both the uniform layer and ring-like deposits provide the film with increased Si (4.6%) and O (34.5%) by depleted Mg content (60.9%) in comparison to the film formed by 70 V. Hence, it can be concluded that the growth of Mg(OH)₂ layer and deposition of Si-enriched phases take place at this stage.

3.3.4.3. Stage 2–3: activation. When the voltage exceeds 190 V, although there is a fluctuation in current density in a voltage range of 190–250 V, the current steadily increases up to 65 mA/cm² at the maximum voltage of 400 V. The film now presents a surface with interconnected nodules which could be formed from a molten phase and featured by a significant amount of fine foam-like pores (Fig. 7, Id). As shown by EDS, there is noticeable increase of Si and O at this stage as well as a depletion of Mg element in the film, providing Si (12.7%), O (54.8%) and Mg (32.2%) in its composition. The film phase composition can be revealed by XRD (Fig. 7, IVa) which shows peaks for periclase (MgO) and brucite (Mg(OH)₂). There is also a hump between 15° and 45° 2θ representing an amorphous constituent, such phase can be enriched with SiO₂.

In the cross-section TEM image (Fig. 7, Va), the film appears compact with localised porosity in some regions and nodular features at the top surface, with some closed pores inside. As shown by the elemental maps (Fig. 7, Vb), O is evenly distributed across the layer thickness, whereas Si content gradually increases towards the film-electrolyte interface, although a Si depleted band can be observed within the top $\sim 1~\mu m$ of the surface layer.

In the GDOES profile (Fig. 7, IIIb), there is a local maximum of H content adjacent to the metal-film interface, which indicates the presence of hydrated phases. Since Mg is concentrated at the inner region depleted by Si (Fig. 7, Vb), the main constituent there is likely to be partially dehydrated Mg(OH)₂. The film-electrolyte interface is enriched by H and Si (Fig. 7, IIIb), thus, the out most part of the film consists mainly of hydrous silicon-containing compounds, which is supported by XPS data, where peaks of Mg 2p at 50.46 eV (Fig. 7, IIc) and Si 2p at 103.13 eV (Fig. 7, IIb) can be resolved, associated with the presence of chemical environment consistent with Mg₃Si₄O₁₀(OH)₂. The crystalline form of this phyllosilicate type compound has a layered structure comprising alternating SiO₄ tetrahedra and MgO₄(OH)₂ octahedra. Raman spectroscopy analysis (Fig. 8) performed to verify this structural arrangement confirms the presence of three spectral regions corresponding to tetrahedral Si-O-Si lattice modes (<500 cm⁻¹), vibration of bridging Si–O–Si bonds (750–600 cm⁻¹) and symmetric stretching vibration of non-bridging Si-O bonds (1100-900 cm⁻¹) in the (Si_xO_y)_z units [41]. Reduced non-bridging signal and pronounced bridging vibration region indicate a likelihood of formation of chain silicate and phyllosilicate structures, the latter including Mg₃Si₄O₁₀(OH)₂ identified by XPS analysis (Fig. 7, IIb, c). However the high fluorescence scattering background, low

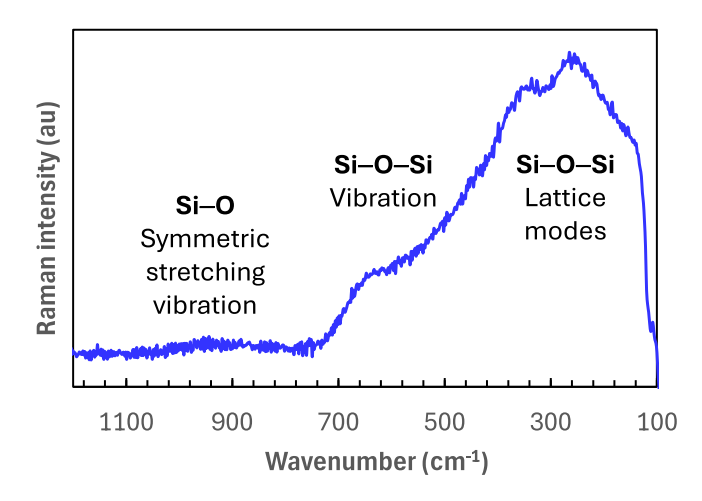


Fig. 8. Raman spectrum of the anodic film formed on cp-Mg in 0.05 M ${\rm Na_2SiO_3}$ solution up to 400 V.

spectral signal-to-noise ratio and absence of well resolved Si-O-Si peaks indicate the lack of long-range order between silicate units and low crystallinity of corresponding compounds. This is consistent with a broad amorphous hump and absence of crystalline silicate phases in the XRD pattern (Fig. 7, IVa). Based on the above findings, we can conclude that for the prebreakdown film, the inner layer mainly consists of a mixture of Mg(OH)₂ and MgO, while the outer region is dominated by a mixture of partly hydrated MgO and SiO₂.

3.3.4.4. Stage 3-4: breakdown. Further increase in the applied voltage (> 400 V) is accompanied by a sharp growth in current density, manifesting the occurrence of dielectric breakdown. The current density reaches the maximum value of 720 mA/cm² at 500 V. At this stage, numerous microdischarges can be easily observed. The resulting film is featured by numerous craters with micro-pores, surrounded by fine granules features $< 2 \mu m$ in size (Fig. 7, Ie). Also, some pores are filled with erupted materials. The film chemical composition remains nearly the same as that formed at the pre-breakdown stage, with a slight increase in Si (15.7%) and O (56.1%) at a decreased Mg content (27.0%). However, there are significant changes in terms of the film phase composition, as revealed by the XRD patterns (Fig. 7, IV). Apart from the increased amount of periclase (MgO), amorphous silicates are present in the resulting film, as indicated by the hump between 15° and 45° 2θ in the XRD pattern (Fig. 7, IVb).

4. Discussion

Our experimental results revealed that anodic behaviour of Mg in the studied electrolyte solutions can be attributed to dissolution-precipitation of several compounds, which occurs at the electrode surface during anodic polarisation. Considering associated changes in local pH and temperature, a solubility analysis of precipitated phases was carried out under variable thermodynamic conditions in the vicinity of Mg anode. Based on this analysis, mechanisms underlying anodic film

Table 1
Solubility products for magnesium compounds in water at 25 °C in stable and active states.

Compound	State	Solubility product (Ks)	pKs = -log(Ks)	Refs.
MgF_2	Stable	5.2E-11	10.3	[37]
MgF_2	Active	6.6E-09	8.2	[36]
$Mg(OH)_2$	Stable	5.6E-12	11.3	[37]
$Mg(OH)_2$	Active	6.3E-10	9.2	[38]
$Mg_3(PO_4)_2$	Stable	6.3E-26	25.2	[37]
$Mg_3(PO_4)_2$	Stable	1.0E-24	24.0	[38]
MgHPO ₄	Stable	1.5E-06	5.8	[36]

evolution during initial stages of PEO treatments in induvial electrolyte systems are elucidated as discussed in subsequent sections.

4.1. Solubility analysis of precipitating phases

Anodic reactions consuming water normally result in anolyte acidification with pH drop being a function of current density and solution buffer capacity [33]. Magnesium can be passivated in aqueous media by direct formation of Mg(OH)₂ only at relatively high pH > 12. Recent attempts to analyse mutual effects of thermodynamic and kinetic factors on anodic behaviour of magnesium as a function of pH in electrolyte solutions relevant to PEO were made by Zhou et al. [32] who operated in terms of solubility constants attributed to stable (aged or calcinated) compounds. However, the solution behaviour of freshly deposited (active) and aged compounds differs significantly (Table 1). Fig. 9 shows that the difference in solubility limits of active and stable Mg(OH)₂ and MgF₂ can reach up to two orders of magnitude. As this work is focused on electrochemical responses of freshly formed films, the solubility products of corresponding compounds in active form will be more appropriate for evaluation of the overall system response at the pre-breakdown stages.

Without external polarisation, electrolyte pH at the electrode vicinity is the same as in the bulk pH⁰ = 13.0 (Fig. 9a, yellow dot). Without passivators, initiation of anodic polarisation results in formation of solid Mg(OH)₂ film by reaction (1) as its solubility at this pH is rather low. However, the release of protons conjugated with anodic reactions (2)-(3) shifts near-surface pH to a lower value (Fig. 9d, red arrow), which increases solubility of Mg(OH)₂ (reaction (4)), resulting in partial activation and significant corrosion of the specimen (Fig. 9b, c). Further local acidification leads to hydrogen evolution following reaction (5). These three scenarios are schematically shown in Fig. 10.

$$Mg_{solid} + 2OH_{soly}^{-} \rightarrow Mg(OH)_{2 \text{ solid}} + 2e$$
 (1)

$$2H_2O \rightarrow O_{2 gas} + 4H_{solv}^+ + 4e$$
 (2)

$$Mg_{solid} + 2H_2O \rightarrow Mg(OH)_{2 solid} + 2H_{solv.}^+ + 2e$$
 (3)

$$Mg(OH)_{2 \text{ solid}} + 2H_{solv.}^{+} \rightarrow Mg_{solv.}^{2+} + 2H_{2}O$$
 (4)

$$Mg_{solid} + 2H_{solv.}^+ \rightarrow Mg_{solv.}^{2+} + H_{2 gas}$$
 (5)

Depending on the synthesis route, dehydration of Mg(OH)₂ occurs at 300–400 °C [42,43]. Dehydration in vacuum or in air is accompanied by formation of a defective partly dehydrated surface layer of Mg(OH)_{2-x}O_{x/2}, which represents a diffusion barrier for water molecules [44,45]. The reverse reaction of hydration easily occurs at room temperature in presence of water. Moreover, hydration of MgO is accompanied by significant volume expansion by about 221% in theory, and even higher in practice because of high degree of porosity in freshly formed Mg(OH)₂ [46]. It is described as a sequence of equilibrium water adsorption followed by reaction step [47]. Thus, the presence of MgO in the coating indicates elevated temperature conditions and the absence of water in this area.

If electrolyte includes fluoride anions the increase in Mg^{2+} concentration due to $Mg(OH)_2$ solubility is limited by a competitive formation of MgF_2 within a wide range of $pH \leq 12.3$ as a noticeable fluoride protonation $(H^+ + F^- = HF)$ occurs only in strong acidic media that are beyond the scope of this work. Solubility of MgF_2 is about two orders of magnitude higher than fresh $Mg(OH)_2$ film at $pH^0 = 13.0$, thus a hypothetical passivation may occur only via the solid-liquid-solid reaction pathway (6)-(7) resulting in reformation of the film into MgF_2 .

$$Mg_{soly}^{2+} + 2F_{soly}^{-} \rightarrow MgF_{2 solid}$$
 (6)

$$Mg(OH)_{2 \text{ solid}} + 2H_{solv.}^{+} + 2F_{solv.}^{-} \rightarrow MgF_{2 \text{ solid}} + 2H_{2}O$$
 (7)

Formation of MgF_2 requires an excess of F in the electrode vicinity, which may be affected by diffusion limitations. It is conceivable that in a situation when the local current density is relatively high, delivery of F from the bulk is limited and actual solubility of magnesium locally increases above the solubility limit of MgF_2 because of a lack in F (Fig. 9d, red line). This would cause local dissolution and decrease in barrier properties of the film leading to localised corrosion.

In contrast to fluoride, phosphate behaviour is more complex because of a series of stepwise protonation reactions (8) [36].

$$PO_4^{3-} + H^+ \rightarrow HPO_4^{2-}$$
 (8.1)

$$HPO_4^{2-} + H^+ \rightarrow H_2PO_4^-$$
 (8.2)

$$H_2PO_4^- + H^+ \rightarrow H_3PO_4$$
 (8.3)

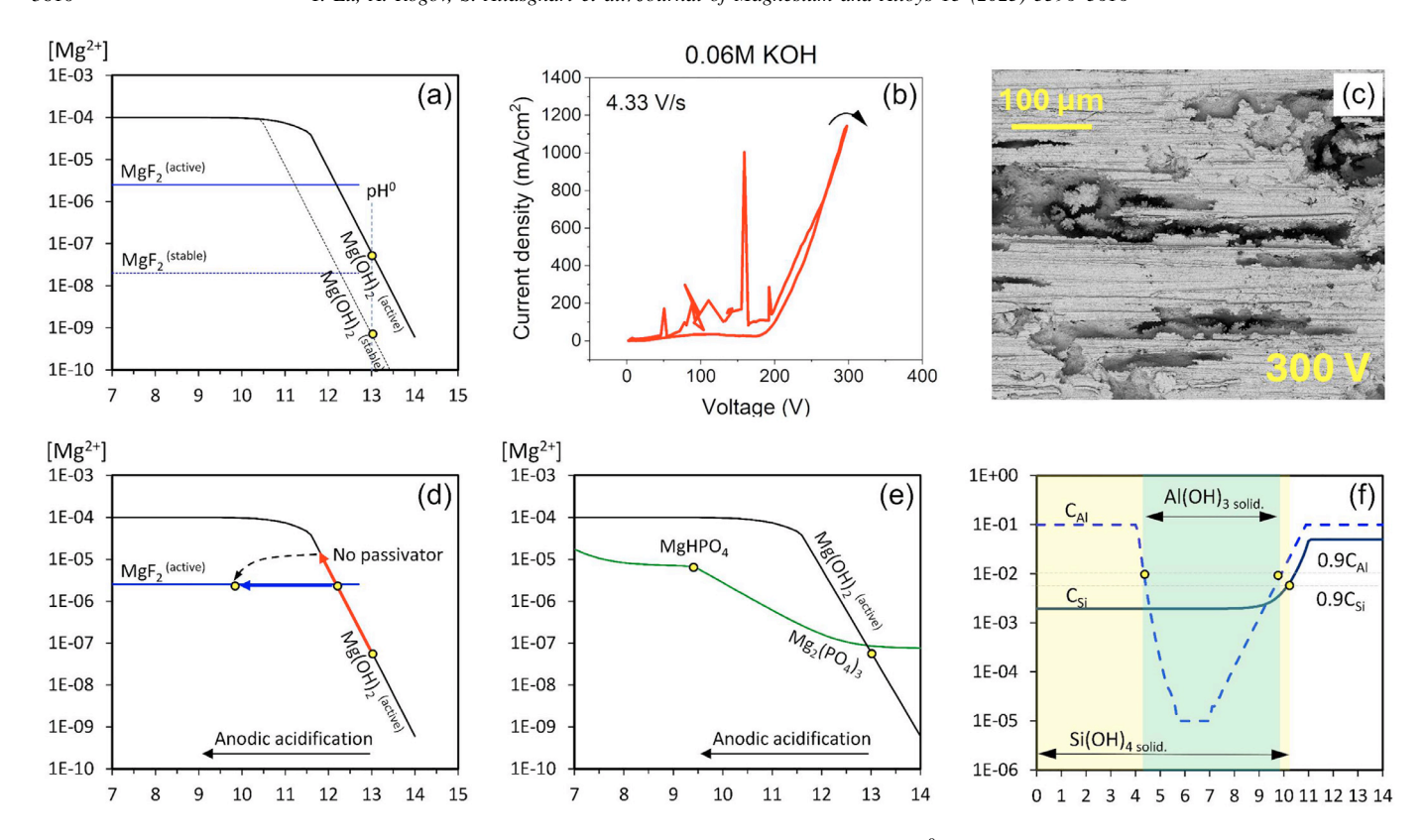


Fig. 9. Comparison of solubility for $Mg(OH)_2$ and MgF_2 in stable (aged) and active (fresh) states. $pH^0=13.0$ corresponds to the bulk solutions used in this work (a); voltammogram for cp-magnesium in 0.06 M KOH electrolyte at the sweep rate of 4.33 V/s (b); SEM surface morphology of the film formed at 300 V. Magnesium speciation as a function of pH in presence of sodium fluoride (d) and trisodium phosphate (e). Equilibrium data for magnesium species $[Mg^{2+}]$ as a result of dissolution of magnesium compounds in water (a, d, e) as functions of pH at 25 °C and the total magnesium concentration 10^{-4} mol/l. Equilibrium data for soluble aluminium (C_{AI}) and silicon (C_{Si}) species. Shaded areas indicate precipitation of solid phases as decrease of initial concentration by 10% (f).

As a result, starting from the same pH⁰=13.0, a local pH decrease due to anodic current leads to a gradual increase in concentration [Mg²⁺] within the region where phosphate species with different protonation degree coexist, as depicted in Fig. 9e. Along this line, film composition varies from pure Mg₃(PO₄)₂ to MgHPO₄. The solubility of MgHPO₄ is even higher than that of MgF₂, therefore it can hardly be considered a suitable passivator.

Anodic behaviour of Mg in silicate and aluminate solutions differs significantly as both of those salts do not form insoluble compounds with magnesium (9)-(11) by coprecipitation, although this is often erroneously mentioned in literature [19,48–54], e.g.:

$$Mg_{solv.}^{2+} + SiO_{3\,solv.}^{2-} \rightarrow MgSiO_{3\,solid} \quad (incorrect)[19], [48] \quad (9)$$

$$2Mg_{solv.}^{2+} + SiO_{3 solv.}^{2-} + H_2O \rightarrow Mg_2SiO_{4 solid} + 2H_{solv.}^+$$
(incorrect)[49], [50] (10)

$$Mg_{solv.}^{2+} + AlO_{solv.}^{2-} \rightarrow MgAl_2O_{4 solid}$$

(incorrect)[51], [52], [53], [54] (11)

Formation of crystalline magnesium silicate (forsterite) or magnesium aluminate (spinel) requires high-temperature sintering (~ 1000 °C) or hydrothermal conditions that cannot

be obtained at the pre-breakdown stage [55,56]. The anodic reaction here results in co-precipitation of amorphous oxo-hydroxide mixture known as magnesium-silicate-hydrate, MgO·SiO₂·H₂O, the stoichiometry of which differs significantly from Mg₂SiO₄ or MgSiO₃ compounds [57–59].

The difference in passivation behaviour of silicate and aluminate electrolytes may be attributed to a different solubility of corresponding oxides on acidification, where hydrated silica is stable for any pH < 10.3, but alumina can be dissolved forming cationic Al³⁺ species if pH decreases below pH 4.2 (Fig. 9f).

Thus, based on the solubility analysis, the films formed in presence of phosphate or fluoride anions are likely to lose stability under anodic acidification, whereas films formed in silicate or aluminate solutions are expected to be more stable.

4.2. Mechanisms underlying initial stages of PEO Mg in basic electrolytes

4.2.1. Aluminate solution

Fig. 11 describes the evolution of surface layer in aluminate electrolyte at different stages corresponding to the voltammogram in Fig. 4, Ia. The initial pH value of the electrolyte is 13, and according to the Pourbaix diagram of Mg [60], at stage $0 \rightarrow 1$ it is passivated forming a thin Mg(OH)₂

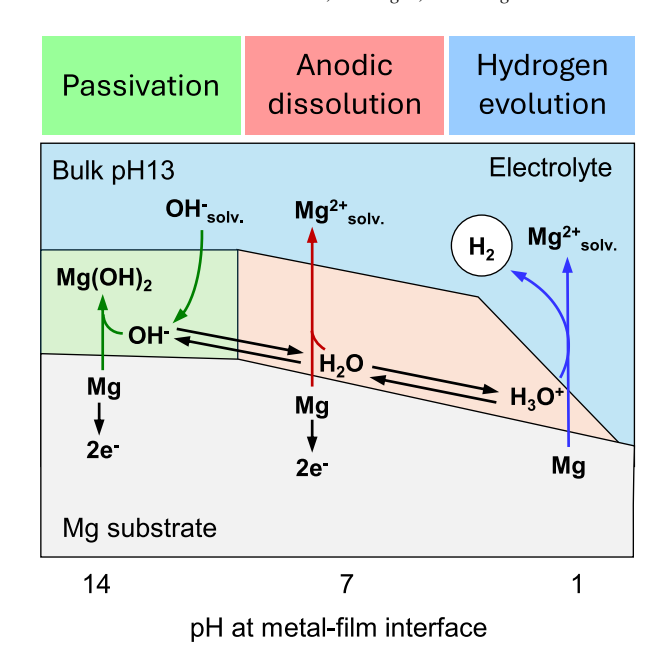


Fig. 10. Magnesium behaviour in alkaline solution without precipitating oxyanion additions as a function of local pH at the metal-film interface, which depends on the anodic current density.

film on the surface by reaction (1). Although this reaction consumes OH^- species, they can still be supplied from the bulk electrolyte. However, this promotes H_2O dissociation, with protons (H^+) being increasingly released and accumulated in the vicinity of the anode, leading to the localised acidification of the environment. This increases the solubility of $Mg(OH)_2$ and reactions (4)-(5) take place. The Mg^{2+} cations may react with $Al(OH)_4^-$ in the electrolyte, depositing $Al(OH)_3$ (reaction (12)).

$$Al(OH)_{4 \text{ solv.}}^{-} \rightarrow Al(OH)_{3 \text{ solid}} + OH_{\text{surf.}}^{-}$$
 (12.1)

$$Mg_{surf.}^{2+} + 2OH_{surf.}^{-} \rightarrow Mg(OH)_{2 \text{ solid}}$$
 (12.2)

At the next stage $(1\rightarrow 2)$, Al(OH)₃ continues to deposit forming the outer part of the film. Since there is an abrupt

increase in the current density during this stage (Fig. 4Ia), we believe that a fresh bare metal may be exposed to the aqueous environment and the anodic dissolution of magnesium substrate occurs, releasing a large number of electrons:

$$Mg \to Mg_{solv}^{2+} + 2e^{-} \tag{13}$$

The reason for the metal exposure might be dehydration of $Mg(OH)_2$ yielding magnesium oxide MgO by reaction (14), which leads to the film shrinkage as evidenced by relative molar volumes of $Mg(OH)_2$ and MgO in respect to that of Mg, 1.73 vs 0.81.

$$Mg(OH)_2 \to MgO + H_2O \tag{14}$$

Since the dehydration of Mg(OH)₂ requires a minimum temperature of 300 °C [42], produced MgO can be regarded as an indicator of temperature developed in the metal-anodic film-electrolyte system at this stage. The Al(OH)₃ layer can be partially dehydrated to boehmite (AlOOH, reaction (15)) which mainly takes place in the region adjacent to Mg(OH)₂ layer underneath at 300 °C [61,62]. However, this temperature is not high enough for the formation of Al₂O₃ which occurs at above 500 °C [63].

$$Al(OH)_3 \rightarrow AlOOH + H_2O$$
 (15)

This may be due to the temperature gradient within the metal-anodic film-electrolyte system. The Al(OH)₃ is formed in the outer region of the surface layer which contacts with the cold electrolyte, and the temperature there may therefore be insufficient to enable its thorough dehydration. Meanwhile, the Al(OH)₃ layer experiences shear stress due to the volume change in the layer underneath, so that it flakes off as shown in SEM image in Fig. 4Ib. This creates an open area which allows the released Mg²⁺ cations to contact with OH⁻ in the alkaline media. During subsequent stage ($2 \rightarrow 3$), the newly formed Mg(OH)₂ covers the exposed substrate, hence current drops.

At the subsequent breakdown stage $(3\rightarrow 4)$, the occurrence of plasma micro-discharges provides localised increases in

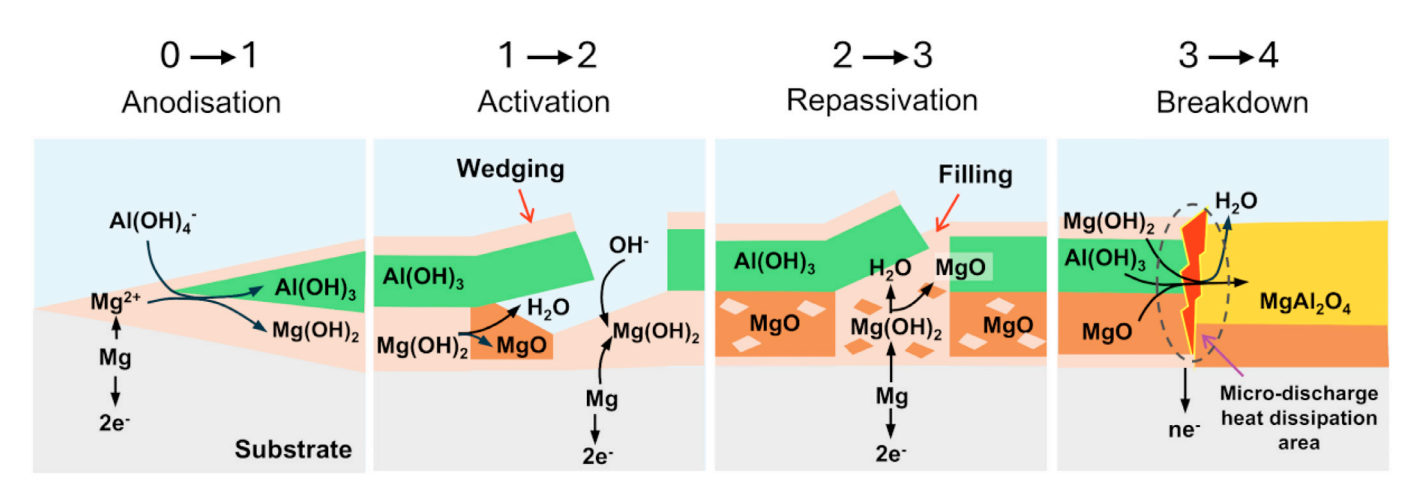


Fig. 11. Schematic illustrating mechanism of plasma electrolytic oxidation process of magnesium in aluminate electrolyte. Each stage corresponds to that shown in the voltammogram in Fig. 4Ia.

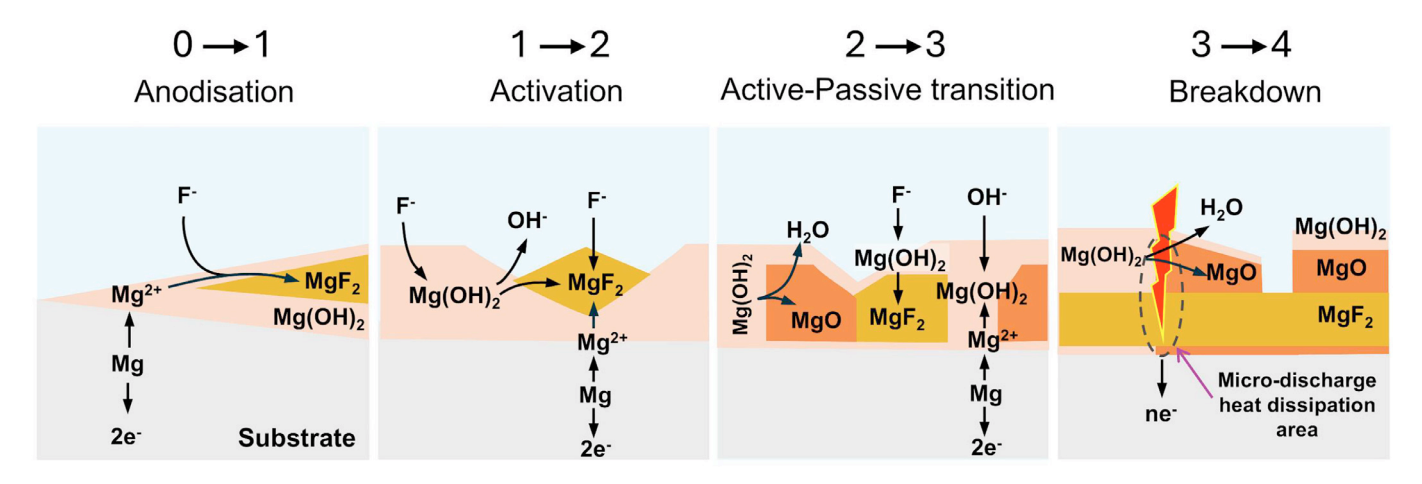


Fig. 12. Schematic illustrating mechanism of plasma electrolytic oxidation process of magnesium in aluminate electrolyte. Each stage corresponds to that shown in the voltammogram in Fig. 5Ia.

high temperature and pressure [64], hence MgAl₂O₄ is formed by sintering:

$$2Al(OH)_3 + MgO \rightarrow MgAl_2O_4 + 3H_2O$$
 (16.1)

$$2Al(OH)_3 + Mg(OH)_2 \rightarrow MgAl_2O_4 + 4H_2O$$
 (16.2)

4.2.2. Fluoride solution

The initial stages of PEO processing of magnesium in fluoride solution are schematically shown in Fig. 12. At the beginning (**stage 0** \rightarrow **1**) the Mg²⁺ cations formed due to Mg(OH)₂ dissolution recombine with F⁻ ions in the vicinity of the anode, resulting in the direct deposition of MgF₂ (reaction (6)) as demonstrated in previous studies [65,66,28].

As the process goes on (stage $1\rightarrow 2$), the release of protons shifts local pH to a lower value triggering deep corrosion of the surface film and underlying Mg substrate. MgF₂ precipitation follows in two pathways as discussed in Section 4.1. It is known that ionic size affects species migration rate under electric field [67]. Since the mobility of F⁻ is greater than that of OH⁻, the fluoride anions attracted to the positively charged Mg anode reach the metal-film interface earlier, forming a MgF₂ layer by direct recombination (reaction (6)) which might be a predominant reaction at this stage.

Subsequent stage $2\rightarrow 3$ involves dehydration of Mg(OH)₂, with metal substrate becoming exposed to electrolyte. This causes magnesium dissolution, releasing Mg²⁺ cations that can encounter OH⁻ and form Mg(OH)₂ which would fill voids in the film. Here deposition of MgF₂ also takes place but preferably by ion exchange (reaction (7)). The F-enriched layer is eventually formed in the vicinity of the metal as explained by Zhu et al. [28] from the viewpoint of crystal structure and dissociation energy. Additionally, the dependence of reaction (7) on the pH value in the vicinity of the anode can change the equilibrium.

When the voltage reaches the breakdown value (stage $3\rightarrow 4$), the dehydration of Mg(OH)₂ becomes the predominant process leading to the significant volume shrinkage of the

coating material, but the film compactness is eventually accomplished by depositing $Mg(OH)_2$ during the voltage rampdown stage.

4.2.3. Orthophosphate solution

Schematic of the film growth in the phosphate electrolyte is shown in Fig. 13. At the initial stage $0\rightarrow 1$, reactions (1)-(4) take place, leading to Mg^{2+} species from $Mg(OH)_2$ to dissolve and react with PO_4^{3-} in the solution, producing $Mg_3(PO_4)_2$:

$$3Mg_{solv.}^{2+} + 2PO_{4 solv.}^{3-} \rightarrow Mg_3(PO_4)_{2 solid}$$
 (17)

This reaction has been widely reported in the literature [68,69,51,70].

As the applied voltage rises (stage $1\rightarrow 2$), the amount of deposited $Mg_3(PO_4)_2$ increases (Fig. 6Ic) and the islands of a granular structure provide pathways for the aqueous media to penetrate towards the underlying layer. This stage involves O_2 evolution (reaction (2)) which results in local acidification and hydration of $Mg_3(PO_4)_2$ via reaction (18).

$$Mg_3(PO_4)_{2 \text{ solid}} + 2H_{\text{soly}}^+ \rightarrow 2MgHPO_{4 \text{ solid}} + Mg_{\text{soly}}^{2+}$$
 (18)

Previous studies [71–73] have also emphasised the presence of MgHPO₄ when magnesium is PEO treated in phosphate electrolytes.

Since the pH level drops at the metal-film interface, the solubility of $Mg(OH)_2$ increases and the released Mg^{2+} cations are repelled by the positively charged substrate, forming fresh $Mg(OH)_2$ when encountering OH^- .

Oxygen evolution continues into stage $2\rightarrow 3$, as concluded from the surface morphology (Fig. 6, Id) showing a number of micro-pores as a sign of gas release accompanied with eruption of Mg₃(PO₄)₂. It should be noted that the outer layer is rather dense and viscous (Fig. 6, Va), which hinders ionic migration; therefore, the released protons are entrapped inside the underlying layer forming MgHPO₄ by reaction (18). At this point, dehydration of Mg(OH)₂ leads to shrinkage of the middle region which exhibits a sponge structure with large pores. At the film-electrolyte interface, previ-

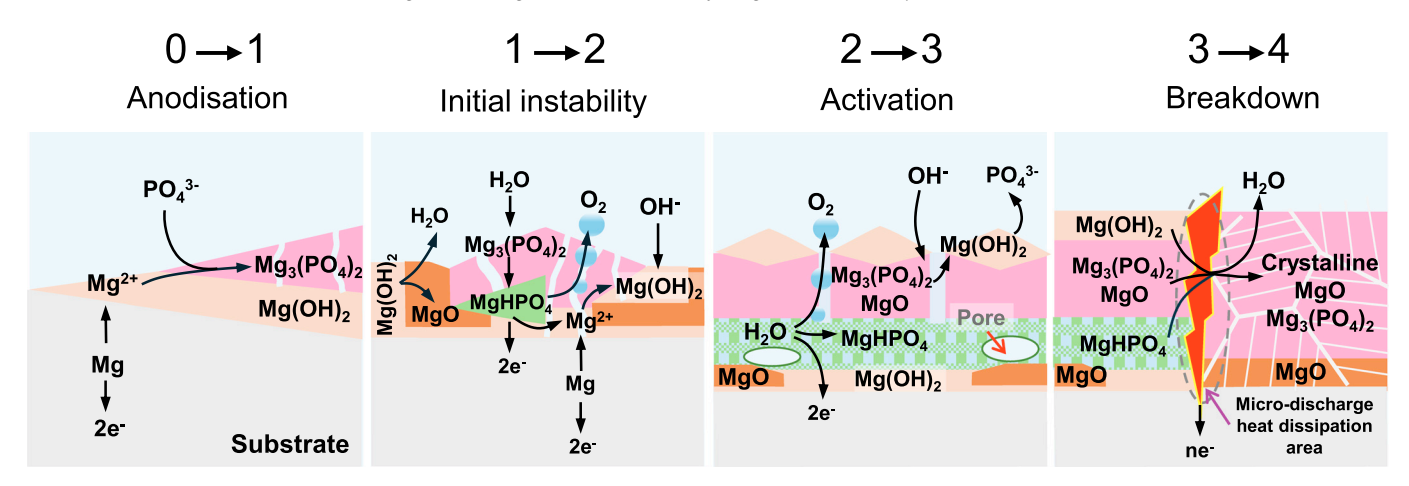


Fig. 13. Schematic illustrating mechanism of plasma electrolytic oxidation process of magnesium in orthophosphate electrolyte. Each stage corresponds to that shown in the voltammogram in Fig. 6Ia.

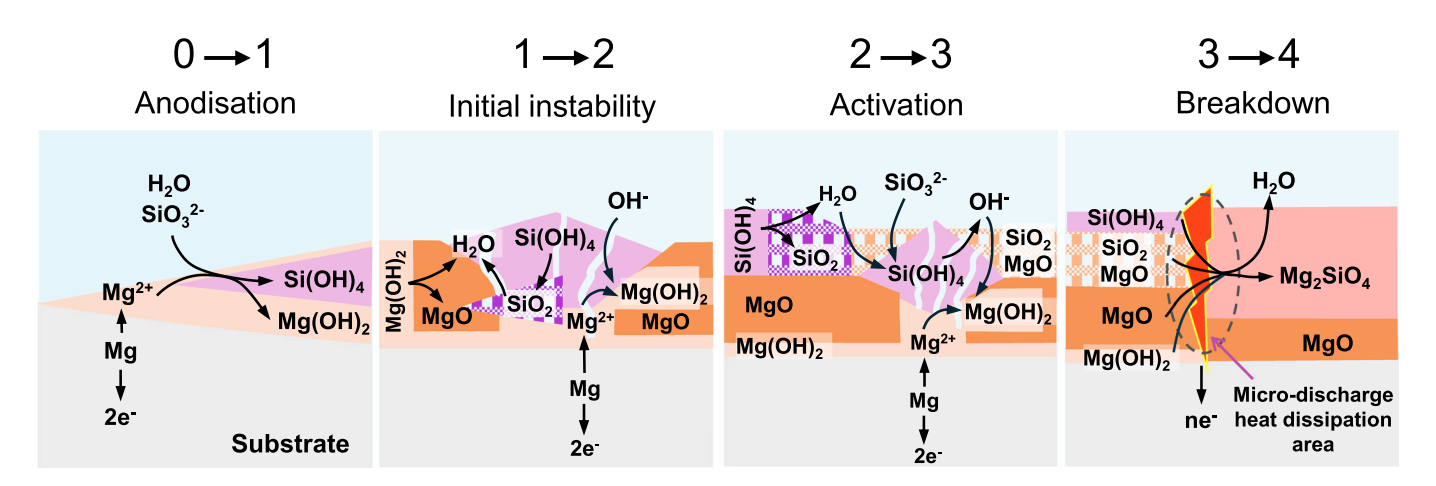


Fig. 14. Schematic illustrating mechanism of plasma electrolytic oxidation process of magnesium in orthophosphate electrolyte. Each stage corresponds to that shown in the voltammogram in Fig. 7Ia.

ously formed $Mg_3(PO_4)_2$ produces $Mg(OH)_2$ by ion exchange in contact with the electrolyte (19):

$$Mg_3(PO_4)_{2 \text{ solid}} + 6OH_{\text{solv.}}^- \rightarrow 3Mg(OH)_{2 \text{ solid}} + 2PO_{4 \text{ solv.}}^{3-} \tag{19}$$

Once breakdown voltage is reached (stage $3\rightarrow 4$), the amorphous $Mg_3(PO_4)_2$ undergoes crystallisation forming crystalline $Mg_3(PO_4)_2$ (farringtonite). Since $Mg_3(PO_4)_2$ cannot further react with MgO [69], these two phases co-exist in the resulting film.

4.2.4. Silicate solution

Film growth in the silicate electrolyte is illustrated as Fig. 14. At stage $0\rightarrow 1$, Si(OH)₄ is precipitated through the following reaction (20):

$$Mg_{solv.}^{2+} + SiO_{3 \text{ solv.}}^{2-} + 3H_2O_{solv.} \rightarrow Si(OH)_{4 \text{ solid}} + Mg(OH)_{2 \text{ solid}}$$
(20)

Apart from the deposition of $Si(OH)_4$, at stage $1\rightarrow 2$, dehydration of $Mg(OH)_2$ also takes place, leading to the shrinkage

of the inner layer, thereby exposing metal substrate. Porosity in the outer Si-rich region provides pathways for diffusion of OH^- and SiO_3^{2-} to react with oxidised magnesium forming fresh $Mg(OH)_2$ and $Si(OH)_4$, respectively. As these hydrated compounds may be subsequently dehydrated, compactness of the inner layer can be achieved by continuous filling of pores with newly formed compounds. Since the migration rate of SiO_3^{2-} is slower than OH^- , $Si(OH)_4$ preferably exists in the outer layer of the film. Similar situation can be observed at stage $2\rightarrow 3$, but the predominant reaction at that stage is likely to be dehydration of $Si(OH)_4$ (reaction (21)) as the surface presents a molten-and-solidified type of morphology indicating development of relatively high temperatures.

$$Si(OH)_4 \rightarrow SiO_2 + 2H_2O \tag{21}$$

Formation of highly disordered phyllosilicate structures in the outer film region is suggested to occur at the pre-breakdown stage by photoelectron and Raman spectroscopy (Fig. 7, IIc, d, Fig. 8). The crystalline Mg₃Si₄O₁₀(OH)₂ compound known as talc is formed under supercritical hydrothermal conditions from metastable magnesium silicate precur-

sors [74]. Apparently, the conditions developed at the filmelectrolyte interface are insufficient to enable long range ordering and crystallisation at this stage, so the surface structure can be represented by a mixture of partly hydrated magnesia and silica units. When the voltage is high enough for breakdown to occur (stage $3\rightarrow 4$) and develop local temperature and pressure sufficient for sintering, the oxo-hydroxide mixture in discharge-affected regions of the film can be transformed into crystalline Mg₂SiO₄:

$$2Mg(OH)_2 + Si(OH)_4 \rightarrow Mg_2SiO_4 + 4H_2O$$
 (22.1)

$$2MgO + SiO_2 \rightarrow Mg_2SiO_4 \tag{22.2}$$

In excess of MgO in the film (Fig. 7, IVa, b), magnesium metasilicate (MgSiO₃) is unlikely be formed as indicated by the phase diagram of MgO-SiO₂ system [75].

5. Conclusions

We have studied anodic behaviour of magnesium at the pre-breakdown stages of PEO process in four aqueous electrolyte systems containing additions of sodium aluminate, fluoride, phosphate and silicate, with initial pH 13. These electrolytes can be categorised into two groups. The first group comprises solutions of aluminate and silicate that passivate Mg surface by direct deposition of insoluble compounds like hydrated alumina or silica – without reaction with anodically dissolved magnesium – but relying on the local pH change in the vicinity of anode surface due to consumption of hydroxyl anions by the anodic reaction. The second group includes solutions of fluoride and phosphate that do require the presence of dissolved Mg²⁺ cations to form solid passivating compounds such as MgF₂ and Mg₃(PO₄)₂.

In the anodic film formed in the fluoride electrolyte, the barrier region adjacent to the metal substrate comprises mainly MgF₂ with rather compact structure. This is different from MgO/Mg(OH)₂ based barrier layers formed in the other three electrolytes, which exhibit less compactness due to partial dehydration. However, the fluoride cannot be used as a sole electrolyte addition because it promotes dissolution of Mg(OH)₂, leading to deep corrosion of Mg substrate. When designing electrolyte systems for PEO processing of Mg, fluorides should therefore be used only in combination with oxyanions such as silicate or aluminate that can passivate metal surfaces by direct precipitation of insoluble compounds as a consequence of anodic process.

Chemical and mechanical instabilities in the MgO/Mg(OH)₂ phase are the main cause of anodic reactivation at the pre-breakdown stages of PEO processing, leading to development of microstructural defects in the growing anodic films on Mg. Chemical instabilities result from increased solubility of MgO and Mg(OH)₂ at reduced pH as well as direct place exchange of hydroxyl groups for anions with a higher affinity to Mg²⁺ (F⁻ in our case). Mechanical instabilities leading to the rupture of the anodic film arise mainly from substantial reduction in volume

during dehydration of Mg(OH)₂ due to high field and local Joule heating. Additionally, stiffer phases in the film (such as AlOOH) may lose their integrity due to undermining caused by dissolution of underlying MgO/Mg(OH)₂ phases. Subsequent repassivation is associated with the increased coverage of metal surface (exposed during reactivation) by insoluble products of the electrochemical anodic process.

Overall, the fundamental understanding of electrochemical behaviour and microstructural evolution of anodic films on cp-Mg during pre-breakdown stages of Plasma Electrolytic Oxidation achieved in this study is expected to provide a useful practical guidance for development of robust electrolyte systems for PEO treatment of magnesium alloys and formation of high-performance protective and functional coatings for a wide range of applications.

CRediT authorship contribution statement

Yuchen Lu: Writing – review & editing, Visualization, Investigation, Formal analysis. Aleksey Rogov: Writing – review & editing, Validation, Methodology, Investigation, Formal analysis. Sepideh Aliasghari: Visualization, Investigation, Formal analysis. Aleksey Yerokhin: Writing – review & editing, Visualization, Supervision, Methodology, Funding acquisition, Formal analysis, Conceptualization.

Acknowledgements

The research leading to this publication was supported by the UK EPSRC (grant EP/T024607/1, 'CoatIN'). The infrastructure enabling this research was provided by the Henry Royce Institute for Advanced Materials, funded through the UK EPSRC grants EP/R00661X/1, EP/S019367/1, EP/P025021/1 and EP/P025498/1 and is acknowledged with thanks. YL acknowledges support from the University of Manchester and Chinese Scholarship Council for his PhD studies. The Authors are grateful to Dr Liam Dwyer help and technical support in XPS studies.

Competing interests

Authors declare that they have no competing interests.

Data availability

All data supporting this study are provided in the main article. Raw data can be made available upon reasonable request. For the purpose of open access, the author has applied a Creative Commons Attribution (CC BY) licence to any Author Accepted Manuscript version arising.

References

- [1] M. Kiani, I. Gandikota, M. Rais-Rohani, K. Motoyama, J. Magnes. Alloys 2 (2014) 99–108.
- [2] Z. Gu, Y. Zhou, Q. Dong, G. He, J. Cui, J. Tan, X. Chen, B. Jiang, F. Pan, J. Eckert, Mater. Sci. Eng.: A. 855 (2022) 143901.

- [3] J. Bai, Y. Yang, C. Wen, J. Chen, G. Zhou, B. Jiang, X. Peng, F. Pan, J. Magnes. Alloys 11 (2023) 3609–3619.
- [4] S.A. Salman, M. Okido, in: Corrosion prevention of magnesium alloys, Woodhead Publishing, Cambridge, 2013, pp. 197–231.
- [5] K. Murakami, M. Hino, T. Kanadani, in: Anodization of Magnesium Alloys Using Phosphate Solution', Magnesium Alloys - Corrosion and Surface Treatments, InTechOpen Ltd, London, 2011, pp. 221–236.
- [6] Q. Li, in: V.S. Saji, T.S.N. Sankara Narayanan, X. Chen (Eds.), Conversion coatings for magnesium and its alloys, Springer International Publishing, Cham, 2022, pp. 415–444.
- [7] A.L. Yerokhin, X. Nie, A. Leyland, A. Matthews, S.J. Dowey, Surf. Coating. Technol. 122 (1999) 73–93.
- [8] Y. Guo, A. Rogov, A. Hird, B. Mingo, A. Matthews, A. Yerokhin, Surf. Coating. Technol. 429 (2022) 127938.
- [9] G. Li, F. Ma, Z. Li, Y. Xu, F. Gao, L. Guo, J. Zhu, G. Li, Y. Xia, Coatings 11 (2021).
- [10] C. Jiang, Y. Wang, S. Wang, Y. Li, Y. Zou, J. Ouyang, D. Jia, Y. Zhou, Surf. Coating. Technol. 444 (2022) 128692.
- [11] H. Li, M. Zhang, X. Wu, Y. Geng, L. Lei, Surf. Coating. Technol. 485 (2024) 130881.
- [12] L. Chai, X. Yu, Z. Yang, Y. Wang, M. Okido, Corros Sci 50 (2008)
- 3274–3279. [13] H. Gao, Q. Li, F.N. Chen, Y. Dai, F. Luo, L.Q. Li, Corros. Sci. 53
- (2011) 1401–1407.[14] S. Aliasghari, T. Hashimoto, P. Kelly, A. Matthews, J. Magnes. Alloys
- 12 (2024) 3589–3601. [15] Y. Ma, X. Nie, D.O. Northwood, H. Hu, Thin Solid Films 469–470 (2004) 472–477.
- [16] F. El-Taib Heakal, A. Mohammed Fekry, M.Ziad Fatayerji, J. Appl. Electrochem. 39 (2009) 583–591.
- [17] D. Veys-Renaux, C.-E. Barchiche, E. Rocca, Surf. Coating. Technol.
- 251 (2014) 232–238. [18] S. Stojadinović, R. Vasilić, J. Radić-Perić, M. Perić, Surf. Coating. Tech-
- nol. 273 (2015) 1–11.
 [19] L. Wang, L. Chen, Z. Yan, H. Wang, J. Peng, J Alloys Compd 480 (2009) 469–474.
- [20] R. Arrabal, A. Pardo, M.C. Merino, M. Mohedano, P. Casajús, E. Matykina, P. Skeldon, G.E. Thompson, Corros. Sci. 52 (2010) 3738–3749.
- [21] M.V. Sidorova, S.L. Sinebrukhov, O.A. Khrisanfova, S.V. Gnedenkov, Phys Procedia 23 (2012) 90–93.
- [22] J. Liang, P.B. Srinivasan, C. Blawert, M. Störmer, W. Dietzel, Electrochim. Acta 54 (2009) 3842–3850.
- [23] M.H. Guerra-Mutis, J.M. Vega, M.I. Barrena, E. Matykina, R. Arrabal, J. Magnes. Alloys 13 (2025) 592–612.
- [24] Y. Akimune, R.C. Bradt, J. Am. Ceramic Soc. 70 (1987) C-84-C-86.
- [25] B. Wei, Y. Cheng, Y. Liu, Z. Zhu, Y. Cheng, Transact. Nonferrous Metals Soc. China 31 (2021) 2287–2306.
- [26] X. Li, X. Liu, B.L. Luan, Appl. Surf. Sci. 257 (2011) 9135-9141.
- [27] A. Heydarian, M. Rahmati, M. Atapour, A. Hakimizad, K. Raeissi, J. Mater. Res. Technol. 27 (2023) 6148–6158.
- [28] L. Zhu, H. Li, Q. Ma, J. Lu, Z. Li, J. Magnes. Alloys 11 (2023) 2823–2832.
- [29] B. Kazanski, A. Kossenko, M. Zinigrad, A. Lugovskoy, Appl Surf Sci 287 (2013) 461–466.
- [30] C.E. Barchiche, D. Veys-Renaux, E. Rocca, Surf. Coating. Technol. 205 (2011) 4243–4248.
- [31] F. Simchen, M. Sieber, T. Lampke, Surf. Coating. Technol. 315 (2017) 205–213.
- [32] P. Zhou, C. Li, G. Jiao, T. Lv, T. Zhang, F. Wang, J. Mater. Sci. Technol. 216 (2025) 66–80.
- [33] M.-K. Zhang, W. Chen, M.-L. Xu, Z. Wei, D. Zhou, J. Cai, Y.-X. Chen, Anal. Chem. 93 (2021) 1976–1983.
- [34] A. Nominé, J. Martin, C. Noël, G. Henrion, T. Belmonte, I.V. Bardin, P. Lukeš, Langmuir 32 (2016) 1405–1409.
- [35] B. Müller, ChemEQL, a program to calculate chemical speciation, version 3.2, Limnological Research Center EAWAG/ETH, CH-6047 Kastanienbaum, Switzerland, 1996.

- [36] A.E. Martell, R.M. Smith, Critical stability constants: inorganic complexes, Plenum Press, Springer, New York, 1976.
- [37] J. Speight, Lange's handbook of chemistry, 16th Edition, 16th ed., Mc-Graw-Hill Education, New York, 2005.
- [38] I. Lambert, H.L. Clever, The solubility of magnesium hydroxide in aqueous systems, in: Alkaline Earth Hydroxides Water Aqueous Solutions, Pergamon, Amsterdam, 1992, pp. 49–111.
- [39] NIST X-ray Photoelectron Spectroscopy DatabaseNIST standard reference database number 20, National Institute of Standards and Technology, Gaithersburg MD, 2000.
- [40] S. Ikonopisov, Electrochim. Acta 22 (1977) 1077-1082.
- [41] A. Wang, J.J. Freeman, B.L. Jolliff, J. Raman Spectroscop. 46 (2015) 829–845.
- [42] H. Slimani, H. Ait Ousaleh, A. El Harrak, M. Linder, A. Faik, Chem. Eng. J. 488 (2024) 151048.
- [43] T. Yoshida, T. Tanaka, H. Yoshida, T. Funabiki, S. Yoshida, T. Murata, J. Phys. Chem. 99 (1995) 10890–10896.
- [44] F. Freund, R. Martens, N. Scheikh-ol-Eslami, J. Therm. Analys. 8 (1975) 525–529.
- [45] M. Hartman, O. Trnka, V. Veselý, AIChE J. 40 (1994) 536-542.
- [46] S.-H. Park, S. Jeon, J. Jang, in: P. Duc Long, N.T. Dung (Eds.), Geotechnics for sustainable infrastructure development, Springer Singapore, Singapore, 2020, pp. 1275–1279.
- [47] Y. Kato, N. Yamashita, K. Kobayashi, Y. Yoshizawa, Appl Therm Eng 16 (1996) 853–862.
- [48] Z. Le, Z. Liu, X. He, Y. Cheng, P. Hu, Y. Cheng, Coatings 13 (2023) 1736.
- [49] S.-Y. Huang, Y.-R. Chu, S.-H. Yang, Y.-L. Lee, Surf. Coating. Technol. 475 (2023) 130164.
- [50] N. Eslamzadeh, R. Ebrahimi-Kahrizsangi, saeed Karbasi, A. Zarebidaki, F. Gharavi, Int. J. Electrochem. Sci. 13 (2018) 6236–6247.
- [51] Gh.Barati Darband, M. Aliofkhazraei, P. Hamghalam, N. Valizade, J. Magnes. Alloys 5 (2017) 74–132.
- [52] Y. Ma, X. Nie, D.O. Northwood, H. Hu, Thin Solid Films 494 (2006) 296–301.
- [53] A. Ghasemi, V.S. Raja, C. Blawert, W. Dietzel, K.U. Kainer, Surf. Coating. Technol. 204 (2010) 1469–1478.
- [54] R.O. Hussein, X. Nie, D.O. Northwood, Electrochim. Acta 112 (2013) 111–119.
- [55] G. Gusmano, P. Nunziante, E. Traversa, G. Chiozzini, J Eur Ceram Soc 7 (1991) 31–39.
- [56] I. Ganesh, Int. Mater. Rev. 58 (2013) 63-112.
- [57] A. Spinthaki, G. Petratos, J. Matheis, W. Hater, K.D. Demadis, Geothermics 74 (2018) 172–180.
- [58] D.R.M. Brew, F.P. Glasser, Cement. Concrete Res. 35 (2005) 85-98.
- [59] I. Bouaoun, H. Hammi, A. Aït-Mokhtar, A. El Amine Hamami, A. M'nif, J. Austral. Ceramic Soc. 53 (2017) 351–359.
- [60] M. Pourbaix, Atlas of Electrochemical Equilibria in Aqueous Solutions, NACE Int, Houston, Texas, 1974.
- [61] Y.O. Leonova, M.A. Sevostyanov, D.O. Mezentsev, D.R. Khayrutdinova, A.S. Lysenkov, J. Phys.: Conference Series 1942 (2021) 012052.
- [62] B.S. Vasile, G. Dobra, S. Iliev, L. Cotet, I.A. Neacsu, V.A. Surdu, A.I. Nicoara, A. Boiangiu, L. Filipescu, Ceramics 4 (2021) 564– 575.
- [63] K. Wefers, C. Misra, in: Oxides and hydroxides of aluminum, 19, Alcoa Laboratories, Pittsburgh, PA, 1987, pp. 1–92.
- [64] A.L. Yerokhin, X. Nie, A. Leyland, A. Matthews, Surf. Coating. Technol. 130 (2000) 195–206.
- [65] Q. Chen, Y. Zheng, S. Dong, X.-B. Chen, J. Dong, Surf. Coating. Technol. 417 (2021) 126883.
- [66] Y. Wang, P. Zhang, Y. Du, W. Zhang, H. Cao, Int. J. Electrochem. Sci. 14 (2019) 10465–10479.
- [67] K. Shimizu, H. Habazaki, P. Skeldon, G.E. Thompson, G.C. Wood, Electrochim. Acta 45 (2000) 1805–1809.
- [68] B. Hadzima, D. Kajánek, M. Jambor, J. Drábiková, M. Březina, J. Buhagiar, J. Pastorková, M. Jacková, Metals (Basel) 10 (2020) 1521.
- [69] C. Yang, P. Chen, W. Wu, L. Sheng, Y. Zheng, P.K. Chu, Coatings 14 (2024) 451.

- [70] A. Fattah-alhosseini, A. Fardosi, M. Karbasi, M. Kaseem, J. Magnes. Alloys 12 (2024) 465–489.
- [71] K. Qian, Q. Dong, Y. Zhang, Y. Shao, Z. Cheng, D. Xia, J. Ju, F. Xue, C. Chu, J. Bai, Appl Surf Sci 629 (2023) 157351.
- [72] W. Zhang, B. Tian, K.-Q. Du, H.-X. Zhang, F.-H. Wang, Int. J. Electrochem. Sci. 6 (2011) 5228–5248.
- [73] Y. Song, D. Shan, R. Chen, F. Zhang, E.-H. Han, Surf. Coating. Technol. 203 (2009) 1107–1113.
- [74] M. Claverie, A. Dumas, C. Carême, M. Poirier, C. Le Roux, P. Micoud, F. Martin, C. Aymonier, Chemistry –Eur. J. 24 (2018) 519–542.
- [75] F. Gu, Z. Peng, H. Tang, L. Ye, W. Tian, G. Liang, M. Rao, Y. Zhang, G. Li, T. Jiang, B. Li, J. Li, S. Ikhmayies, M. Zhang, Y.E. Kalay, J.S. Carpenter, J.-Y. Hwang, S.N. Monteiro, D. Firrao, A. Brown, C. Bai, Z. Peng, J.P. Escobedo-Diaz, R. Goswami, J. Kim, in: Characterization of minerals, metals, and materials 2018, Springer International Publishing, Cham, 2018, pp. 633–642.